Title: Methyl-Metabolite Depletion Elicits Adaptive Responses to Support Heterochromatin Stability and Epigenetic Persistence

Spencer A. Haws[1,2], Deyang Yu[3,4,5], Cunqi Ye[6], Coral K. Wille[1,6], Long C. Nguyen[8,9], Kimberly A. Krautkramer[1,2], Jay L. Tomasiewicz[3], Shany E. Yang[3,4], Blake R. Miller[3,4], Wallace H. Liu[1,2], Kazuhiko Igarashi[8,9], Rupa Sridharan[1,6], Benjamin P. Tu[6], Vincent L. Cryns[3,5,10], Dudley W. Lamming[3,4,5], and John M. Denu[1,2*].

[1]Department of Biomolecular Chemistry, SMPH, University of Wisconsin, Madison, WI, 53706, USA
[2]Wisconsin Institute for Discovery, University of Wisconsin, Madison, WI, 53715, USA
[3]Department of Medicine, SMPH, University of Wisconsin, Madison, WI, 53705, USA
[4]William S. Middleton Memorial Veterans Hospital, Madison, WI, 53705, USA
[5]Molecular & Environmental Toxicology Center, SMPH, University of Wisconsin, Madison, WI, 53705, USA
[6]Department of Biochemistry, University of Texas Southwestern Medical Center, Dallas, TX, 75390, USA
[7]Department of Cell and Regenerative Biology, University of Wisconsin, Madison, WI, 53705, USA
[8]Department of Biochemistry, Tohoku University Graduate School of Medicine, Sendai, 980-8575, JPN
[9]Center for Regulatory Epigenome and Diseases, Tohoku University Graduate School of Medicine, Sendai, 980-8575, JPN
[10]University of Wisconsin Carbone Cancer Center, Madison, WI, 53792, USA

*Correspondence: John M. Denu, john.denu@wisc.edu

Summary

S-adenosylmethionine (SAM) is the methyl-donor substrate for DNA and histone methyltransferases that regulate cellular epigenetic states. This metabolism-epigenome link has been shown to promote the sensitivity of chromatin methylation patterns to altered SAM abundance. However, the adaptive mechanisms that allow cells to actively protect epigenetic information during major fluctuations in SAM availability are unknown. Here, we identify a robust response to SAM depletion that is highlighted by preferential mono-methylation of H3 Lys 9 (H3K9) at the expense of global losses in histone di- and tri-methylation. These coordinated pathways drive *de novo* cytoplasmic and nuclear mono-methylation of H3K9 to preserve heterochromatin stability and support global epigenetic persistence upon metabolic recovery. Conservation of these responses in both young and old mice further support a role for epigenetic adaptation to SAM depletion *in vivo*. Together, these studies provide the first evidence for active epigenetic adaptation and persistence to metabolic stress.

Keywords: metabolism, methionine, SAM, epigenetics, methylation, chromatin, histone, aging, persistence

45 **Introduction**

46

47 Metabolism and the epigenome are connected by central metabolites that act as co-
48 substrates for chromatin modifying enzymes, enabling fluctuations in metabolite availability to
49 directly tune a cell's ability to 'write' and 'erase' chromatin post-translational modifications
50 (PTMs) (Fan et al., 2015; Li et al., 2018). Chromatin methylation has been shown to be
51 particularly susceptible to metabolic perturbations as methyltransferases require a single
52 methyl-donor cofactor, S-adenosylmethionine (SAM) (Ducker and Rabinowitz, 2016; Mentch
53 and Locasale, 2017). For example, accumulation of SAM in *S. cerevisiae* results in global
54 increases in histone methylation levels (Ye et al., 2017). On the contrary, reduced SAM
55 availability has been linked with site-specific losses in histone methylation as well as global
56 depression of DNA methylation in several organisms (Shiraki et al., 2014; Ding et al., 2015; Kera
57 et al., 2013; Tang et al., 2017; Shyh-Chang et al., 2013; Mentch et al., 2015; Tang et al., 2015;
58 Hayashi et al., 2018; Towbin et al., 2012; Strekalova et al., 2019; Wang et al., 2019).
59 Intracellular SAM abundance is dependent on the catalysis of its obligatory precursor
60 metabolite, the essential amino acid methionine (Met). Consumption of popular diets containing
61 low quantities of Met (fish, vegetarian, and vegan) have been shown to significantly correlate
62 with decreased plasma Met concentrations (Farmer, 2014; Schmidt et al., 2016). This link
63 provides an opportunity for diet to directly influence SAM availability. Furthermore, abundance
64 of Met and SAM have both been shown to fluctuate naturally in tune with circadian rhythms
65 (Krishnaiah et al., 2017). Therefore, individuals consuming adequate amounts of dietary Met
66 likely still experience periods of decreased methyl-metabolite availability. While both dietary
67 intake and circadian regulation are capable of influencing Met and SAM abundance, adaptive
68 mechanisms that allow cells to actively respond to – and recover their functional epigenomes
69 from – such metabolic perturbations are unknown. Here, we define the ability of a cell and/or
70 organism to re-establish the epigenome that was present prior to onset of an environmental
71 perturbation or metabolic stress as *epigenetic persistence*.
72 Adaptive mechanisms that respond to methyl-metabolite depletion likely support critical
73 cellular functions under these conditions. Interestingly, dietary Met-restriction is associated with
74 beneficial metabolic reprogramming and lifespan extension in mammals (Orentreich et al., 1993;
75 Yu et al., 2018; Miller et al., 2005; Brown-Borg et al., 2018; Lees et al., 2014; Green and
76 Lamming, 2018). These phenotypes run counter to negative pathologies associated with
77 dysregulated chromatin methylation (i.e., intellectual disability syndromes, cancers, and
78 premature as well as natural aging) (Greer and Shi, 2012). This suggests cells possess

79 responsive mechanisms capable of actively maintaining regulation of site specific and/or global
80 chromatin methylation events during SAM depletion. The goal of this study is to identify and
81 characterize such mechanisms to better understand how organisms actively protect their
82 epigenome in response to fluctuations in central metabolite availability.
83 Here, we identify a robust, conserved chromatin response to metabolically-depleted
84 SAM levels. This cellular response is characterized by global decreases in higher-state histone
85 methylation (di- and tri-methyl) and simultaneous coordinated activation of *de novo* H3K9 mono-
86 methylation involving newly-synthesized and chromatin-bound histone H3. Under extreme
87 conditions of both reduced SAM levels and inhibited methylation that would yield H3K9me1,
88 heterochromatin instability and de-repression of constitutively silenced DNA elements is
89 exacerbated. Acute inhibition of *de* novo H3K9 mono-methylation also leads to the
90 dysregulation of global histone PTM states upon metabolic recovery, disrupting epigenetic
91 persistence to decreased SAM availability. Importantly, chronic metabolic depletion of SAM in
92 both young and old mice recapitulates these *in vitro* findings, revealing a conserved, age-
93 independent chromatin response. These results implicate *de novo* H3K9 mono-methylation as
94 an indispensable mechanism to support heterochromatin stability and global epigenetic
95 persistence in response to SAM depletion.
96
97 **Results**
98
99 Methionine Restriction Stimulates Dynamic Histone PTM Response
100
101 To comprehensively investigate how disruption of methyl-donor metabolism affects
102 chromatin methylation states, global histone proteomics and DNA methylation (5mC) analyses
103 were performed on two distinct *in vitro* and *in vivo* systems. These included Met-restricted
104 HCT116 human colorectal cancer cells and C57BL/6J mouse liver. Methionine metabolism was
105 severely repressed in both systems, highlighted by significant reductions in Met and SAM
106 abundance (Figure 1A and Figure S1A-S1D). Reduced methyl-metabolite availability did not
107 affect global DNA 5mC abundance in either system (Figure 1B-1C). However, LC-MS/MS
108 analysis of more than 40 unique histone H3 peptide proteoforms revealed dynamic PTM
109 responses to Met-restriction in both HCT116 cells and C57BL/6J liver (Figure 1D-1E). In
110 HCT116 cells, Met-restriction stimulated distinct biphasic changes in global PTM profiles (Figure
111 1D). Phase I (0 hr-45 min) was rapid and marked by a trending upregulation of H3K4me2/3,
112 PTMs known to mark transcriptionally active promoters. Phase II (90 min-24 hrs) was

113 characterized by global decreases in di- and tri- histone methylation. Decreased levels of di-
114 and tri-methylated peptides were accompanied by increases in acetylated and unmodified
115 peptide species. Similarly in C57BL/6J mice, histone PTM responses were marked by
116 significant decreases in histone di- and tri-methylation that essentially matched the patterns
117 found in HCT116 cells during the prolonged Phase II response (Figure 1E and Figure S1E-S1J).
118 Decreased higher state (di- and tri-) histone methylation both *in vitro* and *in vivo* highlights a
119 decreased methylation capacity resulting from prolonged Met and/or SAM depletion. Together,
120 these observations suggest perturbed methyl-donor metabolism is capable of stimulating
121 significant changes in histone, but not global 5mC, methylation abundance. Furthermore,
122 similarities between the metabolic and epigenetic responses to Met-restriction across both
123 systems support the use of *in vitro* Met-restriction as a model for mechanistic follow-up studies.
124
125 Decreased SAM Availability Drives Robust Histone Methylation Response
126
127 Dramatic reduction of intracellular Met and SAM correlated with onset of the *in vitro*
128 Phase I and II histone PTM changes, respectively (Figure 1D and Figure S1A-S1B). This
129 implies depletion of individual methyl-metabolites may be capable of stimulating distinct histone
130 modifying pathways. To determine if the global losses in di- and tri- histone methylation *in vitro*
131 are driven specifically by SAM depletion, two alternative approaches were employed to deplete
132 cellular SAM independent of Met (Figure 2A). The first approach utilized RNAi knockdown of the
133 mammalian SAM synthetase MAT2A (methionine adenosyltransferase II alpha). Knockdown via
134 MAT2A-RNAi treatment decreased *MAT2A* transcript abundance by greater than 97%, resulting
135 in a near complete deprivation of SAM availability with no effect on Met levels (Figure 2B-2D).
136 Histone proteomics analysis of MAT2A-RNAi treated cells identified site-specific histone PTM
137 changes that mirrored those identified in HCT116 cells under Phase II Met-restriction conditions
138 ($r=0.778$, $p=8.59e^{-10}$) (Figure 2E). Using a complementary approach, SAM levels were depleted
139 by overexpression of a major SAM consumer, PEMT (phosphatidylethanolamine N-
140 methyltransferase). Ye et al. 2017 have previously shown PEMT overexpression significantly
141 reduces SAM availability in HEK293T human embryonic kidney cells. Histone proteomics
142 analysis of *PEMT* overexpressing HEK293T cells identified site-specific PTM changes that
143 paralleled those of Met-restricted controls ($r=0.803$, $p=3.30e^{-8}$) (Figure 2F). Together, two
144 separate means of reducing SAM levels demonstrate SAM reduction alone is sufficient to inhibit
145 the methylation capacity of a cell, inducing dynamic changes in histone PTM abundance.

146 Furthermore, these findings support the use of prolonged Met-restriction as a model of SAM
147 depletion.
148 The similar changes in global histone PTM abundance across four SAM depletion
149 systems were analyzed for the presence of methyl PTMs whose abundances either increased
150 or were unaffected by this metabolic perturbation. Such PTMs would be candidate mediators of
151 an adaptive response to SAM depletion. Unexpectedly, all four SAM depletion systems
152 exhibited identical changes in H3K9 methylation (Figure 2G-2J). SAM depletion stimulated a
153 decrease in H3K9me2/3 with a corresponding increase in H3K9ac/14ac and unmodified
154 peptides while net H3K9me1 abundance was unchanged. Preservation of net H3K9me1 levels
155 in response to SAM depletion was reproducible in Met-restricted MCF7, HEK-293, Panc1, and
156 HepG2 cell lines, as well as in MAT2A-RNAi treated HepA1 cells (Figure S2A-S2F). The robust
157 conservation of H3K9me1 abundance in diverse systems marked by reduced methylation
158 capacity suggest this PTM may be supported by adaptive, active mechanisms.
159
160 H3K9me1 Abundance under SAM Depletion is Driven by *de novo* Methylation
161
162 Global levels of H3K9me1 could be maintained through two distinct mechanisms during
163 SAM depletion: de-methylation of H3K9me2/3 and/or *de novo* methylation of unmodified H3K9.
164 The decrease in H3K9me2/3 and increase in unmodified H3K9 peptide levels across SAM
165 depletion systems suggest H3K9 can be subjected to facile demethylation while *de novo*
166 methylation appears enzymatically unfavorable. However, *de novo* H3K9 mono-methylation
167 would constitute an active, adaptive response to this metabolic stress that is capable of
168 supporting critical chromatin functions. To investigate the contribution of *de novo* methylation to
169 global H3K9me1 levels, small molecule (UNC0642) inhibition of H3K9 HMTs Ehmt1 and Ehmt2
170 was used to block nuclear H3K9 mono-methylation (Liu F et al., 2013). Small molecule
171 treatment enabled acute inhibition of Ehmt1 and Ehmt2 activity whereas RNAi-mediated
172 repression of H3K9 HMT expression had significant yet minimal effects on H3K9 PTM
173 abundance after 24 hours (Figure S3A-S3D). RNAi treatment was limited to 24 hours as
174 HCT116 cells no longer proliferate beyond 24 hours of Met-restriction (Figure S3E). UNC0642
175 treatment of Met-replete cells significantly reduced H3K9me1 abundance by 35.6% and
176 coupling UNC0642 treatment with Met-restriction stimulated a 20.7% decrease in H3K9me1
177 levels (Figure 3A-3C, Figure S3F). These data suggest Ehmt1/Ehmt2 retain nearly 60% of their
178 H3K9 mono-methylation activity despite severe *in situ* SAM deprivation and that this activity is
179 critical for preserving global H3K9me1 abundance. Furthermore, H3K9me2 abundance

180 decreased significantly in Met-replete cells upon UNC0642 treatment but was unaffected when
181 UNC0642 was coupled with Met-restriction (Figure 3A-3B). This indicates only the mono-
182 methylation activity of Ehmt1 and Ehmt2 is preferentially supported during SAM depletion.
183 In addition to methylation of H3K9 by nuclear enzymes, mono-methylation is known to
184 be enzymatically catalyzed on cytoplasmic histones prior to nuclear import and deposition onto
185 chromatin (Loyola A et al., 2006; Pinheiro et al., 2012). Subcellular fractionation of Met-
186 restricted HCT116 cells coupled with western blot analyses indicated that cytoplasmic
187 H3K9me1 levels increase 3-fold after 24 hours of Met-restriction, with a similar increase in total
188 H3 protein levels (Figure 3D-3E). To determine the contribution of cytoplasmic H3K9me1 to the
189 chromatin-bound nuclear pool after 24 hours of Met-restriction, a pulse-chase, SILAC
190 experiment was performed (Figure 3F). L-Arg^{+10} isotope incorporation prior to Met-restriction
191 was determined to be nearly complete with average incorporation for H3K9 peptides greater
192 than 98% (Figure S3H). Newly synthesized H3 was calculated to comprise 24% of the
193 chromatin bound histone pool and contributed 18% of the global H3K9me1 signal after 24 hours
194 of Met-restriction (Figure 3G-3H). UNC0642 treatment did not significantly lessen the
195 contribution of cytoplasmic H3K9me1 to the total pool, suggesting cytoplasmic H3K9me1 is
196 largely protected from enzyme catalyzed turnover once deposited onto chromatin under these
197 conditions (Figure 3H). Modest, insignificant decreases in L-Arg^{+0} H3K9 PTM signal after
198 UNC0642 treatment can be attributed to reduced incorporation of newly synthesized H3 onto
199 chromatin. (Figure 3G) Reduced H3 incorporation in UNC0642-treated cells is likely the
200 consequence of a slower growth rate under these conditions (Figure S3E). Together, these
201 results suggest ~40% of global H3K9me1 abundance is supported by *de novo* methylation
202 during Met-restriction with nearly equal contributions from both the cytoplasm and nucleus. The
203 remaining ~60% of preserved H3K9me1 levels are likely the result of H3K9me2/3 demethylation
204 (Figure 3I).
205 The significant upregulation of cytoplasmic H3K9me1 and total H3, coupled with their
206 incorporation onto chromatin during SAM depletion, were unexpected. These findings suggest
207 cells utilize scarcely available Met and SAM to support the protein abundance and methylation
208 of histone H3 under these conditions. Shotgun proteomics was performed on cytoplasmic
209 protein fractions of the previously described SILAC experiment to determine if histone protein
210 abundance is uniquely responsive to SAM depletion. Of the more than 2,400 identified proteins,
211 only 8 possessed significant incorporation of the light L-Arg^{+0} isotope and also increased in
212 absolute abundance by a $\log_2$ fold-change value greater than 2.0 (Figure 3J). Frequency of Met
213 residues in the primary amino acid sequence did not affect L-Arg^{+0} isotope incorporation (Figure

214 S3I). Remarkably, all four core histone subunits, Mat2A, and the methionine importer SLC3A2
215 (Bröer et al., 2001) were among the 8 proteins (Figure 3J). These results suggest proteins
216 critical for chromatin stability and methyl-donor metabolism are preferentially generated during
217 metabolically-induced SAM depletion. To our knowledge, this is also the first example of a
218 metabolic stress stimulating increased histone protein abundance.
219
220 H3K9me1 is Redistributed Over Repetitive and Transposable Elements During SAM Depletion
221
222 Multiple, non-redundant mechanisms for H3K9me1 maintenance suggest strong
223 biological pressure exists to retain this PTM under SAM depleted conditions. One critical
224 function for H3K9me1 is to serve as a primer for H3K9me2/3 methylation as methyltransferases
225 that yield these higher methylation states require a mono-methyl substrate (Peters et al., 2001;
226 Loyola et al., 2006; Loyola et al., 2009). Accordingly, installment of H3K9me2/3 for constitutive
227 heterochromatin-mediated repression of telomeric, pericentromeric, and centromeric
228 repetitive/transposable elements requires readily available H3K9me1 (Rea et al., 2000;
229 Bannister et al., 2001; Lachner et al., 2000). Global H3K9me2/3 losses in response to SAM
230 depletion suggest these conditions introduce heterochromatin instability, which would create an
231 increased need for H3K9me1 to restore H3K9me2/3 levels when SAM becomes readily
232 available.
233 To determine if H3K9me1 is being maintained globally or redistributed to regions of
234 susceptible heterochromatin during SAM depletion, ChIP-sequencing was performed. Met-
235 restriction stimulated a 35**%** loss in total H3K9me3 peaks abundance (Figure 4A). A higher
236 percentage of H3K9me3 peaks were lost at LTR, intergenic, and intron annotated loci relative to
237 the total, while H3K9me3 enrichment at satellite, simple repeat, and SINE annotated loci were
238 slightly less sensitive to SAM depletion (Figure 4A). Interestingly, H3K9me1 enrichment at
239 repetitive and transposable loci were either largely unaffected by SAM depletion or increased
240 (Figure 4B). Only the percent change for intergenic and intron annotated H3K9me1 peaks was
241 lost to a greater extent than the total peak number.
242 Maintained or increased levels of H3K9me1 at constitutively repressed regions during
243 SAM depletion could result from the replacement of H3K9me1 for lost H3K9me3. To investigate
244 this possibility, we mapped H3K9me1 reads to regions of lost H3K9me3, and determined that
245 H3K9me1 enrichment increases at 66.4% of nearly $16e^4$ sites (Figure 4C-4D). A higher
246 percentage of these H3K9me1 enriched sites were annotated for LINE, LTR, simple repeat, and
247 satellite elements relative to those experiencing decreased H3K9me1 read enrichment (Figure

248 4E). This indicates H3K9me1 preferentially replaces H3K9me3 at repetitive and transposable
249 loci during SAM depletion. Figure 4F provides a representative image of H3K9me3 replacement
250 by H3K9me1 at a pericentric, repetitive loci. Together, these ChIP-sequencing analyses suggest
251 SAM depletion stimulates the redistribution of H3K9me1 to repetitive and transposable genomic
252 loci which are susceptible to H3K9 demethylation.
253
254 *De novo* H3K9 Mono-methylation Preserves Heterochromatin Stability
255
256 Replacement of H3K9me3 by H3K9me1 may function to preserve heterochromatin
257 stability and pericentric chromatin repression during SAM depletion by providing the primer for
258 site-specific H3K9me2/3 methylation. An MNase accessibility assay was used to evaluate global
259 heterochromatin stability under SAM depleted conditions as MNase can more readily digest
260 euchromatic DNA compared to heterochromatic DNA. Coupling Met-restriction with UNC0642
261 treatment resulted in a significantly greater loss and accumulation of di- and mono-nucleosome
262 species, respectively, compared to Met-restriction alone (Figure 5A-5B). This indicates inhibition
263 of *de novo* H3K9 mono-methylation during SAM depletion has a more detrimental effect on
264 global heterochromatin stability than SAM depletion in isolation. To determine if global
265 decreases in heterochromatin stability resulted in de-repression of transposable DNA elements,
266 RT-qPCR was employed. Transcript abundance of *LINE 1*, *HERV-K*, and *HERV-R* were all
267 significantly elevated after SAM depletion. Coupling SAM depletion with UNC0642 treatment
268 resulted in the further elevation of *LINE1* and *HERV-K* transcript abundance while *HERV-R*
269 expression was unaffected (Figure 5C-5E). Because SAM depletion-induced losses in
270 heterochromatin stability and retrotransposon repression are exacerbated with inhibition of
271 nuclear Ehmt1/2 activity, these data suggest that stimulation of active H3K9 mono-methylation
272 functions, in part, to preserve heterochromatin stability.
273
274 Adaptive H3K9 Mechanisms Support Epigenetic Persistence Upon Metabolic Recovery
275
276 Dysregulation of adaptive epigenetic mechanisms during SAM depletion may produce
277 aberrant changes in histone PTMs that compromise long-term epigenetic persistence upon
278 metabolic recovery. To determine if *de novo* H3K9me1 is required for epigenetic persistence to
279 SAM depletion, HCT116 cells were allowed to recover in Met-replete media after being
280 subjected to Met-restriction coupled with acute vehicle control or UNC0642 treatment (Figure
281 6A). Histone proteomics analysis confirmed that inhibition of Ehmt1/2 activity during SAM

282 depletion results in a significant loss of H3K9me1 abundance (Figure 6B-6C). Upon 5 and 24
283 hours of Met-repletion, vehicle control cells largely regained the original histone PTM state
284 (Figure 6B). However, histone PTM states of UNC0642 cells acutely treated only during Met-
285 restriction remained dysregulated after both 5 and 24 hours of Met-repletion (Figure 6B).
286 Although significant global dysregulation was apparent, the H3K9 peptide proteoforms displayed
287 the most dynamic differences (Figure 6D-6E). Interestingly, the signature H3K9 PTM response
288 to SAM depletion described in Figure 3 was largely retained upon Met-repletion in cells acutely
289 treated with UNC0642 (Figure 6D-6E). H3K9me3 abundance was an exception, recovering to
290 levels consistent with regained *LINE 1* and *HERV-K/R* repression (Figure 5C-5E).
291 To assess the transcriptional consequences of lost epigenetic persistence, RNA-
292 sequencing was performed on cells which recovered in Met-replete media after Met-restriction
293 coupled with acute vehicle control or UNC0642 treatment. Principle Component Analysis (PCA)
294 of normalized Transcripts Per Million (TPM) values produced 3 distinct clusters, suggesting
295 altered epigenomes correlate with altered transcript profiles in these cells (Figure 6F). A multiple
296 condition comparison analysis was used to determine which transcripts distinguished the
297 clusters from one another (Figure 6G). While 68.4% of identified genes were ubiquitously
298 expressed across samples (Pattern 1), 27.7% were uniquely expressed in control cells relative
299 to both recovery groups (Pattern 4) (Figure 6H). This result supports the PCA findings as the
300 pre-restriction control group is most distinct from both recovery groups. Unique gene expression
301 profiles for UNC0642 (Pattern 2) and DMSO (Pattern 3) recovery cells contained 1.9% and
302 0.7%, respectively, of all identified genes. Therefore, these subsets of genes are responsible for
303 the unique clustering of both Met-restriction recovery groups (Figure 6H). Gene Set Enrichment
304 Analysis (GSEA) was performed on both Pattern 2 and 3 gene lists to determine functional
305 differences between each gene set. GSEA of Pattern 2 genes identified 71 significantly enriched
306 gene ontology (GO) terms possessing an FDR q-value less than 0.25, while an identical
307 analysis of Pattern 3 genes did not identify any significantly enriched GO terms (Figure 6I-6J).
308 Of the significantly enriched GO terms in Pattern 2, 66 possessed a positive Normalized
309 Enrichment Score (NES) when comparing UNC0642 to vehicle control recovery cells (Figure
310 S4A-S4B). Figure 6K is a representative GSEA running enrichment score figure of a GO term
311 possessing a positive NES. Only 5 of the significantly enriched GO terms in Pattern 2
312 possessed a negative NES when comparing UNC0642 to vehicle control recovery cells.
313 Notably, a majority of the genes assigned to these GO terms were zinc finger binding proteins
314 (Figure S4C-S4D). Figure 6L is a representative GSEA running enrichment score figure of a GO
315 term possessing a negative NES.

316 These data suggest adaptive regulation of H3K9 PTMs in response to SAM depletion is
317 required for long-term epigenetic persistence upon metabolic recovery. Furthermore, inhibited
318 epigenetic persistence results in significant transcriptional consequences that impact a diverse
319 set of cellular functions.
320
321 Adaptive and Persistent Epigenetic Responses to SAM Depletion are Robust *in vivo*,
322 Independent of Age
323
324 To determine if adaptive and persistent responses to SAM depletion exist *in vivo* and are
325 age-dependent, 6- and 22-month C57BL/6J mice were subjected to 3 weeks of Met-restriction
326 followed by 5 weeks of Met-repletion (Figure 7A). Several previous reports have associated
327 decreased H3K9me2/3 abundance with aging in numerous organisms (Wood et al., 2010;
328 Larson et al., 2012; Ni et al., 2012; Tvardovskey et al., 2017; Scaffidi and Misteli, 2006). Age-
329 dependent dysregulation of heterochromatin has been associated with de-repression of
330 repetitive DNA and transposable elements, as well as DNA damage, factors which may
331 contribute to disease progression (Wood et al., 2016; De Cecco et al., 2013; De Cecco et al.,
332 2019; Oberdoerffer and Sinclair, 2007; Booth and Brunet, 2016). Therefore, conservation of
333 both adaptive and persistent responses to SAM depletion across the lifespan would further
334 support the functional importance of both mechanisms as an "older" chromatin environment is
335 thought to be inherently dysregulated.
336 Remarkably, histone proteomics analysis of liver tissue revealed H3K9 was the only
337 residue on which PTMs responded similarly to SAM depletion in both 6- and 22-month mice
338 relative to age matched controls (Figure 7B). This PTM response at H3K9 phenocopied those
339 identified in the previously described *in vitro* and whole-organism SAM depletion studies, further
340 highlighting the robust regulation of this residue (Figure 7C). Significant age-dependent
341 responses to SAM depletion were identified on all remaining histone residues (Figure 7B and
342 S5A-S5E). Furthermore, significantly elevated *LINE 1*, *SINE B1*, and *SINE B2* transcript
343 abundance in both 6- and 22-month mice suggest the chromatin instability phenotype
344 characterized in Figure 5 also occurs during metabolic depletion of SAM *in vivo* (Figure 7D-7E).
345 After 5 weeks of dietary Met-reintroduction, both young and old mice displayed the ability to re-
346 establish an epigenome similar to that possessed by age-matched controls (Figure 7B).
347 Interestingly, 22-month mice appeared to more rapidly adopt the control histone PTM state,
348 while the 6-month mice still exhibited residual losses in H3K9me3 and increases in H3K9me1
349 after 5 weeks of recovery (Figure 7F). Consistent with the general recovery of chromatin states,

350 both age groups largely reestablished repression of *LINE 1*, *SINE B1*, and *SINE B2* expression
351 (Figure 7G-7H).
352 Metabolic changes in young and old mice tracked with H3K9 PTMs. Both 6- and 22-
353 month mice in the Met-restriction group experienced significant losses in total body weight
354 relative to age matched controls (Figure S5F). Decreases in overall body weight were
355 comprised of significant losses in both lean and fat mass (Figure S5F). Altered body-weight and
356 compositions were accompanied by significantly improved glucose tolerance in both young and
357 old mice (Figure S5G). Upon Met-repletion, mice reacquired their initial metabolic state in an
358 age-independent manner. All animals experienced significant increases in total body weight,
359 comprised of elevated lean and fat mass, as well normalized glucose tolerance relative to age-
360 matched controls (Figure S5H-S5I).
361 Together, strong association of the H3K9 chromatin response to SAM depletion with
362 metabolic reprogramming in young and old mice suggest H3K9 regulatory mechanisms are not
363 only robust across lifespan but may be required to support these metabolic phenotypes.
364 Furthermore, these data show the ability of epigenetic states to persist upon recovery from a
365 metabolic challenge is an inherent property of both isolated cells and complex mammals.
366
367 **Discussion**
368 Here, we provide a comprehensive investigation into the adaptive regulation of
369 chromatin during a metabolic stress. A highly conserved, robust histone methylation response to
370 SAM depletion was discovered, characterized by global losses in histone H3 di- and tri-
371 methylation while H3K9me1 is actively maintained to safeguard against exacerbated
372 heterochromatin instability and support epigenetic persistence upon metabolic recovery. These
373 mechanisms involve the enrichment of H3K9me1 in susceptible regions of heterochromatin
374 through *de novo* methylation on both chromatin-bound and cytoplasmic H3. To our knowledge,
375 this is the first identified mechanism in which scarce, diet-derived nutrients are funneled toward
376 the preservation of specific chromatin PTM states.
377 Zee et al., 2010 have previously determined H3K9me1 has the shortest half-life of 17
378 measured PTMs, highlighting the importance of *de novo* methylation for supporting global
379 H3K9me1 abundance in a SAM depleted environment. Here, *de novo* methylation was found to
380 be critical for more than simply sustaining global H3K9me1 levels under these conditions. ChIP-
381 sequencing analyses determined H3K9me1 experiences a significant redistribution across
382 heterochromatin and enrichment at repetitive and transposable DNA elements, particularly in
383 regions where H3K9me3 is lost. Redistribution of H3K9me1 to these regions is likely critical for

384 preserving heterochromatin as prevention of *de novo* H3K9 mono-methylation resulted in global
385 losses in heterochromatin stability and site-specific retrotransposon de-repression. We
386 hypothesize H3K9me1 mediates repression of retrotransposons during SAM depletion by acting
387 as a substrate for HMTs which deposit di- and tri-methyl PTMs onto H3K9. (Peters et al., 2001;
388 Loyola et al., 2006; Loyola et al., 2009; Rea et al., 2000; Bannister et al., 2001; Lachner et al.,
389 2000). This function is not limited to nuclear derived H3K9me1. Pinheiro et al., 2012 have
390 previously shown inhibition of cytoplasmic H3K9 mono-methylation through shRNA knockdown
391 of *PRDM3* and *PRDM16* stimulates pericentric heterochromatin loss and disruption of the
392 nuclear lamina. Our study demonstrates cytoplasmic derived H3K9me1 comprises a significant
393 portion (18%) of the total chromatin bound pool after 24 hours of Met-restriction *in vitro*.
394 Adaptation of H3K9 mono-methylation to SAM depletion is also critical for long-term epigenetic
395 persistence to this metabolic stress. Prevention of *de novo* H3K9 mono-methylation during SAM
396 depletion resulted in sustained dysregulation of global histone PTMs upon metabolic recovery,
397 significantly influencing gene expression patterns. This requirement for an active, adaptive
398 histone PTM response to support epigenetic persistence upon metabolic recovery is the first
399 identified mechanism of its kind.
400 Replication of *in vitro* results *in vivo*, independent of age, strongly supports the discovery
401 of a universal adaptive and persistent response to SAM depletion. Here, we demonstrate that
402 the adaptive mechanisms required to support H3K9me1-mediated heterochromatin stability are
403 inducible in both 6- and 22-month mice after dietary Met-restriction. Furthermore, H3K9me1
404 maintenance under SAM depleted conditions uniquely correlated with beneficial metabolic
405 reprogramming (i.e. reduced fat mass and improved glucose tolerance) in both young and old
406 mice. This suggests the robust regulation of H3K9 PTMs in response to SAM depletion may be
407 required to support the metabolic reprogramming stimulated by dietary Met-restriction. Global
408 epigenetic persistence to metabolic SAM depletion was also identified in both 6- and 22-month
409 mice. Validation of this phenomenon *in vivo*, independent of age, suggests similar mechanisms
410 critical for maintaining proper regulation of the epigenome during natural fluctuations in the
411 availability of other metabolic cofactors may exist as well. Such fluctuations could be stimulated
412 by periods of prolonged fasts, chronic intake of foods lacking essential cofactors (i.e. vegan and
413 vegetarian dietary patterns), and circadian regulated changes in metabolite availability (Farmer,
414 2014; Schmidt et al., 2016; Krishnaiah et al., 2017).
415 Notably, we did not observe an age-associated decrease in H3K9 methylation between
416 6- and 22-month control diet mice (Table S1). Similar regulation of H3K9 PTMs and mirrored
417 metabolic responses to SAM depletion across age groups suggest our 22-month mice, the

418 equivalent to a 60-70 year old human, have not yet experienced a decline in health span
419 (Flurkey et al., 2007). It will be interesting to determine if the adaptive and persistent epigenetic
420 mechanisms revealed here are functional in very old animals (i.e. >30 months) where H3K9
421 methylation is thought to be inherently dysregulated. Disruption of these mechanisms later in an
422 organism's lifespan could support age-associated de-repression of transposable elements
423 (Wood et al., 2016; De Cecco et al., 2013; Oberdoerffer and Sinclair, 2007; Booth and Brunet,
424 2016), contributing to negative phenotypes that accelerate the aging process such as
425 inflammation (De Cecco et al., 2019; Simon et al., 2019).
426 Future studies will be needed to determine how H3K9 mono-methyltransferases are able
427 to maintain their catalytic activity in SAM depleted environments. Favorable steady-state kinetic
428 constants for H3K9me1 relative to H3K9me2/3 HMTs is one possibility. However, it is difficult to
429 address this hypothesis by comparing current H3K9 HMT enzymology data due to varied
430 selections of substrates and assays. Direct shuttling of SAM to H3K9me1 HMTs by Mat2A could
431 also support H3K9me1 catalytic activity. As SAM is energetically expensive to produce, due to
432 the 1:1 requirement of Met and ATP molecules for its synthesis, in addition to being highly
433 unstable (Wu et al., 1983), it would be advantageous for the cell to possess mechanisms which
434 permit preferential shuttling of SAM during methyl-metabolite depletion. Directed SAM
435 production and utilization have been proposed in other metabolic contexts (Katoh et al., 2011;
436 Kera et al., 2013; Li et al., 2015).
437
438 **Acknowledgements**
439
440 This research was supported in part by grants from the NIH (S.A.H. –T32 DK007665; K.A.K.
441 T32 DK007665; W.H.L. T32 DK007665; J.M.D. – R37 GM059785; D.W.L. – AG041765,
442 AG050135, AG051974, AG056771, AG062328, a New Investigator Program Award (D.W.L.)
443 and a Collaborative Health Sciences Program Award (V.L.C.) from the Wisconsin Partnership
444 Program, the V. Foundation for Cancer Research (V.L.C.), and a Glenn Foundation Award for
445 Research in the Biological Mechanisms of Aging (D.W.L.), as well as startup funds from the
446 UW-Madison School of Medicine and Public Health and the UW-Madison Department of
447 Medicine (V.L.C. and D.W.L.). This research was conducted while D.W.L. was an AFAR
448 Research Grant recipient from the American Federation for Aging Research. D.Y. is supported
449 in part by a fellowship from the American Heart Association (17PRE33410983). The Lamming
450 laboratory is supported in part by the U.S. Department of Veterans Affairs (I01-BX004031), and
451 this work was supported using facilities and resources from the William S. Middleton Memorial

Veterans Hospital. This work does not represent the views of the Department of Veterans Affairs or the United States Government. We would like to thank Alexis J. Lawton for the bioinformatics analysis presented in Figure S3I. We would also like to thank the University of Wisconsin-Madison Biotechnology Center and the University of Wisconsin-Madison Center for High Throughput Computing for their help in generating and analyzing the ChIP-sequencing data presented in Figure 5, respectively.

Author Contributions

Conceptualization, S.A.H., D.W.L, V.L.C., and J.M.D.; Methodology, S.A.H., C.Y., C.K.W., L.N.C., W.H.L., K.I., B.P.T., D.W.L., and J.M.D.; Validation, S.A.H., D.Y., C.Y., L.N.C., K.A.K., K.I., B.P.T., D.W.L., and J.M.D.; Formal Analysis, S.A.H., D.Y., C.K.W., K.A.K., D.W.L., and J.M.D; Investigation, S.A.H., D.Y., C.Y., L.N.C., K.A.K., J.L.T., S.E.Y., and B.R.M.; Resources, K.I., B.P.T., V.L.C., D.W.L., and J.M.D.; Writing – Original Draft, S.A.H. and J.M.D.; Writing – Review & Editing, S.A.H., D.Y., C.Y., C.K.W., W.H.L., K.I., R.S., B.P.T., V.L.C., D.W.L., and J.M.D.; Visualization, S.A.H., D.Y., and D.W.L.; Supervision and Project Administration, K.I., R.S., B.P.T., D.W.L., and J.M.D.; Funding Acquisition, S.A.H., K.I., R.S., B.P.T., V.L.C., D.W.L., and J.M.D.

Declaration of Interests

J.M.D. is a consultant for FORGE Life Sciences and co-founder of Galilei BioSciences. D.W.L has received funding from, and is a scientific advisory board member of, Aeonian Pharmaceuticals, which seeks to develop novel, selective mTOR inhibitors for the treatment of various diseases. Remaining authors declare no competing interest.

478 **References**

479

480 1. Arriola Apelo, S.I., Neuman, J.C., Baar, E.L., Syed, F.A., Cummings, N.E., Brar, H.K.,
481 Pumper, C.P., Kimple, M.E., and Lamming, D.W. (2016) Alternative rapamycin treatment
482 regimens mitigate the impact of rapamycin on glucose homeostasis and the immune
483 system. Aging Cell. 15, 28-38.
484 2. Bannister, A.J., Zegerman, P., Pardridge, J.F., Miska, E.A., Thomas, J.O., Allshire, R.C.,
485 and Kouzarides, T. (2001) Selective recognition of methylated lysine 9 on histone H3 by
486 the HP1 chromo domain. Nature. 410, 120-124.
487 3. Bolger, A.M., Lohse, M., and Usadel, B. (2014) Trimmomatic: a flexible trimmer for
488 Illumina sequence data. Bioinformatics. 30, 2114-2120.
489 4. Booth, L.N. and Brunet, A. (2016) The aging epigenome. Mol. Cell. 62, 728-744.
490 5. Bröer, A., Friedrich, B., Wagner, C.A., Fillon, S., Ganapathy, V., Lang, F., and Bröer, S.
491 (2001) Association of 4F2hc with light chains LAT1, LAT2 or y+LAT2 requires different
492 domains. Biochem J. 355, 735-731.
493 6. Brown-Borg, H.M., Rakoczy, S., Wonderlich, J.A., Borg, K.E., and Rojanathammanee, L.
494 (2018) Metabolic adaptation of short-living growth hormone transgenic mice to
495 methionine restriction and supplementation. Ann. N.Y. Acad. Sci. 1418, 118-136.
496 7. Clasquin, M.F., Melamud, E., and Rabinowitz, J.D. (2012) LC-MS processing with
497 MAVEN: a metabolomic analysis and visualization engine. Curr. Protoc. Bioinformatics.
498 Chapter 14, Unit 14.11. doi:10.1002/0471250953.bi1411s37.
499 8. Cox, J., Hein, M.Y., Luber, C.A., Paron, I., Nagaraj, N., and Mann, M. (2014) Accurate
500 proteome-wide label-free quantification by delayed normalization and maximal peptide
501 ratio extraction, termed MaxLFQ. Mol. Cell Proteomics. 13, 2513-2526.
502 9. De Cecco, M., Criscione, S.W., Peckham, E.J., Hillenmeyer, S., Hamm, E.A.,
503 Manivannan, J., Peterson, A.L., Kreiling, J.A., Neretti, N., and Sedivy, J.M. (2013)
504 Genomes of replicatively senescent cells undergo global epigenetic changes leading to
505 gene silencing and activation of transposable elements. Aging Cell. 12, 247-256.
506 10. De Cecco, M., Ito, T., Petrashen, A.P., Elias, A.E., Skivr, N.J., Criscione, S.W.,
507 Caligiana, A., Brocculi, G., Adney, E.M., Boeke, J.D., Le, O., Beauséjour, C., Ambati, J.,
508 Ambati, K., Simon, M., Seluanov, A., Gorbunova, V., Slagboom, P.E., Helfand, S.L.,
509 Neretti, N., and Sedivy, J.M. (2019) L1 drives IFN senescent cells and promotes age-
510 associated inflammation. Nature. 566, 73-78.

511 11. Ding, W., Smulan, L.J., Hou, N.S., Taubert, S., Watts, J.L., and Walker, A.K. (2015) S-
512 adenosylmethionine levels govern innate immunity through distinct methylation-
513 dependent pathways. Cell Metab. 22, 633-645.
514 12. Ducker, G.S. and Rabinowitz, J.D. (2017) One-carbon metabolism in health and
515 disease. Cell Metab. 25, 27-42.
516 13. Fan, J., Krautkramer, K.A., Feldman, J.L., and Denu, J.M. (2015) Metabolic regulation of
517 histone post-translational modifications. ACS Chem. Biol. 10, 95-108.
518 14. Farmer, B. (2014) Nutritional adequacy of plant-based diets for weight management:
519 observations from the NHANES. Am. J. Clin. Nutr. 100 Suppl 1, 365S-368S.
520 15. Flurkey, K., Currer, J.M., and Harrison, D.E. (2007) The Mouse in Aging Research. In
521 the Mouse in Biomedical Research 2nd Edition. Fox, J.G., et al., editors. American
522 College Laboratory Animal Medicine (Elsevier), pp. 637-671.
523 16. Green, C.L. and Lamming, D.W. (2018) Regulation of metabolic health by essential
524 dietary amino acids. Mech. Ageing Dev. S0047-6374(18)30079-4. doi:
525 0.1016/j.mad.2018.07.004.
526 17. Greer, E.L. and Shi, Y. (2012) Histone methylation: a dynamic mark in health, disease,
527 and inheritance. Nat. Rev. Genet. 13, 343-357.
528 18. Hardies, S.C., Wang, L., Zhou, L., Zhao, Y., Casavant, N.C., and Huang, S. (200) LINE-
529 1 (L1) lineages in the mouse. Mol. Biol. Evol. 17, 616-628.
530 19. Hayashi, T., Teruya, T., Chaleckis, R., Morigasaki, S., and Yanagida, M. (2018) S-
531 adenosylmethionine synthetase is required for cell growth, maintenance of G0 phase,
532 termination of quiescence in fission yeast. iScience 5, 38-51.
533 20. Heinz, S., Benner, C., Spann, N., Bertolino, E., Lin, Y.C., Laslo, P., Cheng, J.X., Murre,
534 C., Singh, H., and Glass, C.K. (2010) Simple combinations of lineage-determining
535 transcription factors prime cis-regulatory elements required for macrophage and B cell
536 identities. Mol. Cell. 38, 576-589.
537 21. Kang, Y.K., Park, J.S., Lee, C.S., Yeom, Y.I., Chung, A.S., and Lee, K.K. (1999) Efficient
538 integration of short interspersed element-flanked foreign DNA via homologous
539 recombination. J. Biol. Chem. 274, 36585-36591.
540 22. Katoh, Y., Ikura, T., Hoshikawa, Y., Tashiro, S., Ito, T., Ohta, M., Kera, Y., Noda, T., and
541 Igarashi, K. (2011) Methionine adenosyltransferase II serves as a transcriptional
542 corepressor of Maf oncoprotein. Mol. Cell. 41, 554-566.

543 23. Kera, Y., Katoh, Y., Ohta, M., Matsumoto, M., Takano-Yamamoto, T., and Igarashi, K.
544 (2013) Methionine adenosyltransferase II-dependent histone H3K9 methylation at the
545 COX-2 gene locus. J. Biol. Chem. 288, 13592-13601.
546 24. Klawitter, S., Fuchs, N.V., Upton, K.R., Upton, K.R., Muñoz-Lopez, M., Shukla, R.,
547 Wang, J., Garcia-Cañadas, M., Lopez-Ruiz, C., Gerhardt, D.J., Sebe, A., Grabundzija, I.,
548 Merkert, S., Gerdes, P., Pulgarin, J.A., Bock, A., Held, U., Witthuhn, A., Haase, A.,
549 Sarkadi, B., Löwer, J., Wolvetang, E.J., Martin, U., Ivics, Z., Izsvák, Z., Garcia-Perez,
550 J.L., Faulkner, G.J., and Schumann, G.G. (2016) Reprogramming triggers endogenous
551 L1 and Alu retrotransposition in human induced pluripotent stem cells. Nat. Commun.
552 7:10286. doi: 10.1038/ncomms10286.
553 25. Konze, K.D., Ma, A., Li, F., Barsyte-Lovejoy, D., Parton, T., Macnevin, C.J., Liu, F., Gao,
554 C., Huang, X.P., Kuznetsova, E., Rougie, M., Jiang, A., Pattenden, S.G., Norris, J.L.,
555 James, L.I., Roth, B.L., Brown, P.J., Frye, S.V., Arrowsmith, C.H., Hahn, K.M., Wang,
556 G.G., Vedadi, M., and Jin, J. (2013) An orally bioavailable chemical probe of lysine
557 methyltransferases EZH2 and EZH1. ACS Chem. Biol. 8, 1324-1334.
558 26. Krishnaiah, S.Y., Wu, G., Altman, B.J., Growe, J., Rhoades, S.D., Coldren, F.,
559 Venkataraman, A., Olarerin-George, A.O., Francey, L.J., Mukherjee, S., Girish, S.,
560 Selby, C.P., Cal, S., Er, U., Sianati, B., Sengupta, A., Anafi, R.C., Kavakli, I.H., Sancar,
561 A., Baur, J.A., Dang, C.V., Hogenesch, J.B., and Weljie, A.M. (2017) Clock regulation of
562 metabolites reveals coupling between transcription and metabolism. Cell Metab. 35,
563 961-974.
564 27. Lachner, M., O'Carroll, D., Rea, S., Mechtler, K., and Jenuwein, T. (2001) Methylation of
565 histone H3 lysine 9 creates a binding site for HP1 proteins. Nature. 410, 116-120.
566 28. Larson, K., Yan, S.J., Tsurumi, A., Liu, J., Zhou, J., Gaur, K., Guo, D., Eickbush, T.H.,
567 and Li, W.X. (2012) Heterochromatin formation promotes longevity and represses
568 ribosomal RNA synthesis. PLoS Genet. 8, e1002473. doi:
569 10.1371/journal.pgen.1002473.
570 29. Lees, E.K., Król, E., Grant, L., Shearer, K., Wyse, C., Moncur, E., Bykowska, A.S.,
571 Mody, N., Gettys, T.W., and Delibegovic, M. (2014) Methionine restriction restores a
572 younger metabolic phenotype in adult mice with alterations in fibroblast growth factor 21.
573 Aging Cell. 13, 817-827.
574 30. Leng, N., Dawson, J.A., Thomson, J.A., Ruotti, V., Rissman, A.I., Smits, B.M., Haag,
575 J.D., Gould, M.N., Stewart, R.M., and Kendziorski, C. (2013) EBSeq: an empirical Bayes
576 hierarchical model for inference in RNA-seq experiments. Bioinformatics. 29, 1035-1043.

577 31. Li, H., Handsaker, B., Wysoker, A., Fennell, T., Ruan, J., Homer, N., Marth, G.,
578 Abecasis, G., Durbin, R., and 1000 Genome Project Data Processing Subgroup. (2009)
579 The sequence alignment/map format and SAMtools. Bioinformatics. 25, 2078-2079.
580 32. Li, B. and Dewey, C.N. (2011) RSEM: accurate transcript quantification from RNA-Seq
581 data with or without a reference genome. BMC Bioinform. doi: 10.1186/1471-2105-12-
582 323.
583 33. Li, S., Swanson, S.K., Gogol, M., Florens, L., Washburn, M.P., Workman, J.L, and
584 Suganuma, T. (2015) Serine and SAM responsive complex SESAME regulates histone
585 modification crosstalk by sensing cellular metabolism. Mol. Cell. 60, 408-421.
586 34. Li, X., Egervari, G., Wang, Y., Berger, S.L., and Lu, Z. (2018) Regulation of chromatin
587 and gene expression by metabolic enzymes and metabolites. Nat. Rev. Mol. Cell Biol.
588 19, 563-578.
589 35. Liu, F., Barsyte-Lovejoy, D., Li, F., Xiong, Y., Korboukh, V., Huang, X.P., Allali-Hassani,
590 A., Janzen, W.P., Roth, B.L., Frye, S.V., Arrowsmith, C.H., Brown, P.J., Vedadi, M., and
591 Jin, J. (2013) Discovery of an in vivo chemical probe of the lysine methyltransferases
592 G9a and GLP. J. Med. Chem. 56, 8931-8942.
593 36. Loyola, A., Bonaldi, T., Roche, D., Imhof, A., and Almouzni, G. (2006) PTMs on H3
594 variants before chromatin assembly potentiate their final epigenetic state. Mol. Cell. 24,
595 309-316.
596 37. Loyola, A., Tagami, H., Bonaldi, T., Roche, D., Quivy, J.P., Imhof, A., Nakatani, Y., Dent,
597 S.Y. and Almouzni, G. (2009) The HP1α-CAF1-SETDB1-containing complex provides
598 H3K9me1 for Suv39-mediated K9me3 in pericentric heterochromatin. Embo Rep. 10,
599 769-775.
600 38. MacLean, B., Tomazela, D.M., Shulman, N., Chamber, M., Finney, G.L., Frewen, B.,
601 Kern, R., Tabb, D.L., Liebler, D.C., and MacCoss, M.J. (2010) Skyline: an open source
602 document editor for creating and analyzing targeted proteomics experiments.
603 Bioinformatics. 26, 966-968.
604 39. Mauger, O., Klinck, R., Chabot, B., Muchardt, C., Allemand, E., and Batsché, E. (2015)
605 Alternative splicing regulates the expression of G9A and SUV39H2 methyltransferases,
606 and dramatically changes SUV39H2 functions. Nucleic Acids Res. 43, 1869-1882.
607 40. Melamud, E., Vastag, L, and Rabinowitz, J.D. (2010) Metabolomic analysis and
608 visualization engine for LC-MS data. Anal. Chem. 82, 9818-9826.
609 41. Mentch S.J. and Locasale J.W. (2016) One-carbon metabolism and epigenetics:
610 understanding the specificity. Ann N. Y. Acad. Sci. 1363, 91-98.

611 42. Mentch, S.J., Mehrmohamadi, M., Huang, L., Liu, X., Gupta, D., Mattocks, D., Gómez
612 Padilla, P., Ables, G., Bamman, M.M., Thalacker-Mercer, A.E. Nichenametla, S.N., and
613 Locasale, J.W. (2015) Histone methylation dynamics and gene regulation occur through
614 the sensing of one-carbon metabolism. Cell Metab. 22,861-873.
615 43. Miller, R.A., Buehner, G., Chang, Y., Harper, J.M., Sigler, R., and Smith-Wheelock, M.
616 (2005) Methionine-deficient diet extends mouse lifespan, slows immune and lens aging,
617 alters glucose, T4, IGF-I and insulin levels, increases hepatocyte MIF levels and stress
618 resistance. Aging Cell. 4, 119-125.
619 44. Mootha, V.K., Lindgren, C.M., Eriksson, K.F., Subramanian, A., Sihag, S., Lehar, J.,
620 Puigserver, P., Carlsson, E., Ridderstråle, M., Laurila, E., Houstis, N., Daly, M.J.,
621 Patterson, N., Mesirov, J.P., Golub, T.R., Tamayo, P., Spiegelman, B., Lander, E.S.,
622 Hirschhorn, J.N., Altshuler, D., and Groop, L.C. (2003) PGC-1alpha responsive genes
623 involved in oxidative phosphorylation are coordinately downregulated in human diabetes.
624 Nat. Genet. 34, 267-273.
625 45. Ni, Z., Ebata, A., Alipanahiramandi E., and Lee, S.S. (2012) Two SET domain containing
626 genes link epigenetic changes and aging in Caenorhabditis elegans. Aging Cell. 11, 315-
627 325.
628 46. Northcott, P.A., Nakahara, Y., Wu, X., Feuk, L., Ellison, D.W., Croul, S., Mack, S.,
629 Kongkham, P.N., Peacock, J., Dubuc, A., Ra, Y.S., Zilberberg, K., Mcleod, J., Scherer,
630 S.W., Rao, J.S., Eberhart, C.G., Grajkowska, W., Gillespie, Y., Lach, B., Grundy, R.,
631 Pollack, I.F., Hamilton, R.L., Van Meter, T., Carlotti, C.G., Boop, F., Bigner, D.,
632 Gilbertson, R.J., Rutka, J.T., and Taylor, M.D. (2009) Multiple recurrent genetic events
633 converge on control of histone lysine methylation in medulloblastoma. Nat. Genet. 41,
634 465-472.
635 47. Oberdoerffer, P. and Sinclair, D.A. (2007) The role of nuclear architecture in genome
636 instability and ageing. Nat. Rev. Mol. Cell Biol. 8, 692-702.
637 48. Orentreich, N., Matias, J.R., DeFelice, A., and Zimmerman, J.A. (1993) Low methionine
638 ingested by rats extends life span. J. Nutr. 123, 269-274.
639 49. Peters, A.H., O'Carroll, D., Scherthan, H., Mechtler, K., Sauer, S., Schöfer, C.,
640 Weipoltshammer, K., Pagani, M., Lachner, M., Kohlmaier, A., Opravil, S., Doyle, M.,
641 Sibilia, M., and Jenuwein, T. (2001) Loss of the Suv39h histone methyltransferase
642 impairs mammalian heterochromatin and genome stability. Cell. 107, 323-327.
643 50. Pinheiro, I., Margueron, R., Shukeir, N., Eisold, M., Fritzsch, C., Richter, F.M., Mittler, G.,
644 Genoud, C., Goyama, S., Kurokawa, M., Son, J., Reinberg, D., Lachner, M., and

645 Jenuwein, T. (2012) Prdm3 and Prdm16 are H3K9me1 methyltransferases required for
646 mammalian heterochromatin integrity. Cell. 150, 948-960.
647 51. Qi, F., Shang, K., Zhang, J., Chuai, S., Kong, D., Zhou, T., Fu, S., Liang, Y., Li, C.,
648 Chen, Z., Zhao, Y., Yu, Z., Huang, Z., Hu, M., Ying, H., Chen, Z., Zhang, Y., Xing, F.,
649 Zhu, J., Xu, H., Zhao, K., Lu, C., Atadja, P., Xia, Z.X., Li, E., and Shou, J. (2015) Histone
650 methyltransferase SETDB1 regulates liver cancer cell growth through methylation of
651 p53. Nat. Commun. 6, 8651.
652 52. Quinlan, A.R. and Hall, I.M. (2010) BEDTools: a flexible suite of utilities for comparing
653 genomic features. Bioinformatics. 26, 841-842.
654 53. Rea S., Eisenhaber, F., O'Carroll, D., Strahl, B.D., Sun, Z.W., Schmid, M., Opravil, S.,
655 Mechtler, K., Pontin, C.P., Allis, C.D., and Jenuwein, T. (2000) Regulation of chromatin
656 structure by site-specific histone H3 methyltransferases. Nature. 406, 593-599.
657 54. Rhyu, D.W., Kang, Y.J., Ock, M.S., Eo, J.W., Choi, Y.H., Kim, W.J., Leem, S.H., Yi, J.M.,
658 Kim, H.S., and Cha, H.J. (2014) Expression of human endogenous retrovirus env genes
659 in the blood of breast cancer patients. Int. J. Mol. Sci. 15, 9173-9183.
660 55. Scaffidi, P. and Misteli, T. (2006) Lamin A-dependent nuclear defects in human aging.
661 Science. 312, 1059-1063.
662 56. Schmidt, J.A., Rinaldi, S., Scalber, A., Ferrari, P., Achaintre, D., Gunter, M.J., Appleby,
663 P.N., Key, T.J., and Travis, R.C. (2016) Plasma concentrations and intakes of amino
664 acids in male meat-eaters, fish-eaters, vegetarians and vegans: a cross-sectional
665 analysis in EPIC-Oxford cohort. Eur. J. Clin. Nutr. 70, 306-312.
666 57. Shiraki, N., Shiraki, Y., Tsuyama, T., Obata, F., Miura, M., Nagae, G., Aburatani, H.,
667 Kume, K., Endo, F., and Kume, S. (2014) Methionine metabolism regulates maintenance
668 and differentiation of human pluripotent stem cells. Cell Metab. 19, 780-794.
669 58. Shyh-Chang, N., Locasale, J.W., Lyssiotis, C.A., Zheng, Y., Teo, R.Y.,
670 Ratanasirintrawoot, S., Zhang, J., Onder, T., Unternaehrer, J.J., Zhu, H., Asara, J.M.,
671 Daley, G.Q., and Cantley, L.C. (2013) Influence of threonine metabolism on S-
672 adonsylmethionine and histone methylation. Science. 339, 222-226.
673 59. Simon, M., Van Meter, M., Ablaeva, J., Ke, Z., Gonzalez, R.S., Taguchi, T., De Cecco,
674 M., Leonova, K.I., Kogan, V., Helfand, S.L., Neretti, N., Roichman, A., Cohen, H.Y.,
675 Meer, M.V., Gladyshev, V.N., Antoch, M.P., Gudkov, A.V., Sedivy, J.M., Seluanov, A.,
676 and Gorbunova, V. (2019) LINE1 derepression in aged wild-type and SIRT6-deficient
677 mice drives inflammation. Cell Metab. 29, 871-885.

678 60. Strekalova, E., Malin, D., Weisenhorn, E.M.M., Russell, J.D., Hoelper, D., Jain, A., Coon,
679 J.J., Lewis, P.W., and Cryns, V.L. (2019) S-adenosylmethionine biosynthesis is a
680 targetable metabolic vulnerability of cancer stem cells. Breast Cancer Res. Treat. 175,
681 39-50.
682 61. Subramanian, A., Tamayo, P., Mootha, V.K., Mukherjee, S., Ebert, B.L., Gillette, M.A.,
683 Paulovich, A., Pomeroy, S.L., Golub, T.R., Lander, E.S., and Mesirov, J.P. (2005) Gene
684 set enrichment analysis: a knowledge-based approach for interpreting genome-wide
685 expression profiles. Proc. Natl. Acad. Sci.102, 15545-15550.
686 62. Tang, S., Fang, Y., Huang, G., Xu, X., Padilla-Banks, E., Fan, W., Xu, Q., Sanderson,
687 S.M., Foley, J.F., Dowdy, S., McBurney, M.W., Fargo, D.C., Williams, C.J., Locasale,
688 J.W., Guan, Z., and Li, X. (2017) Methionine metabolism is essential for SIRT1-regulated
689 mouse embryonic stem cell maintenance and embryonic development. EMBO J. 36,
690 3175-3193.
691 63. Tang, X., Keenan, M.M., Wu, J., Lin, C.A., Dubois, L., Thompson, J.W., Freedland, S.J.,
692 Murphy, S.K., and Chi, J.T. (2015) Comprehensive profiling of amino acid response
693 uncovers unique methionine-deprived response dependent on intact creatine
694 biosynthesis. PLoS Genet. 11, e1005158. doi: 10.1371/journal.pgen.1005158.
695 64. Towbin, B.D., González-Aguilera, C., Sack, R., Gaidatzis, D., Kalck, V., Meister, P.,
696 Askjaer, P., and Gasser, S.M. (2012) Step-wise methylation of histone H3K9 positions
697 heterochromatin at the nuclear periphery. Cell. 150, 934-937.
698 65. Tvardovskiy, A., Schwämmle, V., Kempf, S.J., Rogowska-Wrzesinska, A., and Jensen,
699 O.N. (2017) Accumulation of histone variant H3.3 with age is associated with profound
700 changes in histone methylation landscape. Nucleic Acids Res. 45, 9272-9289.
701 66. Wang, Z., Yip, L.Y., Lee, J.H.J., Wu, Z., Chew, H.Y., Chong, P.K.W., Teo, C.C., Ang,
702 H.Y.K., Peh, K.L.E., Yuan, J., Ma, S., Choo, L.S.K., Basri, N., Jiang, X., Yu, Q., Hillmer,
703 A.M., Lim, W.T., Lim, T.K.H., Takano, A., Tan, E.H., Tan, D.S.W., Ho, Y.S., Lim, B., and
704 Tam, W.L. (2019) Methionine is a metabolic dependency of tumor-initiating cells. Nat.
705 Med. 25, 825-837.
706 67. Watson, G.W., Wickramasekara, S., Palomera-Sanchez, Z., Black, C., Maier, C.S.,
707 Williams, D.E., Dashwood, R.H., and Ho, E. (2014) SUV39H1/H3K9me3 attenuates
708 sulforaphane-induced apoptotic signaling in PC3 prostate cancer cells. Oncogenesis. 3,
709 e131.

710 68. Wood, J.G., Hillenmeyer, S., Lawrence, C., Chang, C., Hosier, S., Lightfoot, W.,
711 Mukherjee, E., Jiang, N., Schorl, C., Brodsky, A.S., Neretti, N., and Helfand, S.L. (2010)
712 Chromatin remodeling in the aging genome of Drosophila. Aging Cell. 9, 971-978.
713 69. Wood, J.G., Jones, B.C., Jiang, N., Chang, C., Hosier, S., Wickremesinghe, P., Garcia,
714 M., Harnett, D.A., Burhenn, L., Neretti, N., and Helfand, S.L. (2016) Chromatin-modifying
715 genetic interventions surpress age-associated transposable element activation and
716 extend life span in *Drosophila*. Proc. Natl. Acad. Sci. 113, 11277-11282.
717 70. Wu, S.E., Huskey, W.P., Borchardt, R.T., and Schowen, R.L. (1983) Chiral instability at
718 the sulfur of S-adenosylmethionine. Biochemistry. 22, 2828-2832.
719 71. Ye, C., Sutter, B.M., Wang, Y., Kuang, Z., and Tu, B.P. (2017) A metabolic function for
720 phospholipid and histone methylation. Mol. Cell 66, 180-193.
721 72. Yu, D., Yang, S.E., Miller, B.R., Wisinski, J.A., Sherman, D.S., Brinkman, J.A.,
722 Tomasiewicz, J.L., Cummings, N.E., Kimple, M.E., Cryns, V.L., and Lamming, D.W.
723 (2018) Short-term methionine deprivation improves metabolic health via sexually
724 dimorphic, mTORC-1 independent mechanisms. FASEB J. 32, 3471-3482.
725 73. Zhang, Y., Liu, T., Meyer, C.A., Eeckhoute, J., Johnson, D.S., Bernstein, B.E.,
726 Nusbaum, C., Myers, R.M., Brown, M., Li, W., and Liu, X.S. (2008) Model-based
727 analysis of ChIP-Seq (MACS). Genome Biol. 9, R137. doi: 10.1186/gb-2008-9-9-r137.
728 74. Zee, B.M., Levin, R.S., Xu, B., Leroy, G., Wingreen, N.S., and Garcia, B.A. (2010) In
729 vivo residue-specific histone methylation dynamics. J. Biol. Chem. 285, 3341-3350.
730

731 **Main Figure Titles and Legends**

732

733 Figure 1. Methionine Restriction Stimulates Dynamic Histone PTM Response

734

735 *(*A) Metabolic pathway diagram illustrating changes in Met-cycle metabolite abundance after 24
736 hours and 5 weeks of Met-restriction in HCT116 cells and C57BL/6J liver, respectively. n=5,
737 error bars represent SD, *p<0.05 (Welch's t-Test). (*B-C*) Plots illustrating global, relative 5mC
738 DNA methylation levels during Met-restriction. n≥3, error bars represent SD, *p<0.05 (Welch's t-
739 Test) (*D-E*) Hierarchichal clustered heatmaps of LC-MS/MS generated log_2 fold-change
740 stoichiometric histone H3 peptide proteoform values relative to 0-hour or chow diet controls in
741 HCT116 cells and C57BL/6J liver, respectively. n≥3, *p<0.05, **p<.01 (Welch's t-Test). See
742 also Table S1 and Figure S1.

743

744 Figure 2. Decreased SAM Availability Drives Robust Histone Methylation Response

745

746 (*A*) Pathway diagram illustrating experimental approaches to depleting intracellular SAM
747 availability. (*B*) Bar graph of relative *MAT2A* mRNA abundance in HCT116 cells as measured
748 by RT-qPCR. n≥2, error bars represent SD, *p<0.05 (Welch's t-Test). (*C-D*) Dot plots of relative
749 Met and SAM levels in HCT116 cells. n≥4, *p<0.05 (Welch's t-test). (*E-F*) Correlation plot of LC-
750 MS/MS generated log_2 fold-change stoichiometric values for individual histone H3 peptide
751 proteoforms. n=3. (*G*-J) Bar graphs illustrating LC-MS/MS generated log_2 fold-changes for
752 individual H3K9 PTMs. n=3 *p<0.05 (Welch's t-test) See also Table S1, Table S2, and Figure
753 S2.

754

755 Figure 3. H3K9me1 Abundance under SAM Depletion is Driven by *de novo* Methylation

756 (*A-B*) Bar graphs illustrating LC-MS/MS generated log_2 fold-changes for individual H3K9 PTMs
757 in HCT116 cells. n≥2, error bars represent SD, *p<0.05 (Welch's t-Test). (*C*) Bar graph
758 illustrating percent loss in global H3K9me1, as measured by LC-MS/MS, in response to 5μm
759 UNC0642 treatment. n≥2, error bars represent SD, *p<0.05 (Welch's t-Test) (*D*) Scatter plot of
760 relative, total H3 and H3K9me1 cytoplasmic protein abundance in HCT116 cells as measured
761 by western blot. Error bars represent SD, n=3, *p<0.05 (Welch's t-Test). (*E*) Representative
762 western blot images of those used for the quantification presented in Figure 3E. Alpha-Tubulin
763 is used as a cytoplasm marker to confirm efficient sub-cellular fractionation. See Document S1
764 for REVERT Total Protein Stain images used for normalization. (*F*) Diagram illustrating the

765 SILAC experimental design. (*G*) Bar graph illustrating contribution of newly synthesized histone
766 H3 to the total chromatin bound pool after 24 hours of Met-restriction in HCT116 cells as
767 measured by LC-MS/MS. n≥2, error bars represent SD, *p<0.05 (Welch's t-test). (*H*) Bar graph
768 illustrating ratio of light:heavy L-Arg isotope presence in H3K9 proteoforms after 24 hours of
769 Met-restriction in HCT116 cells as measured by LC-MS/MS. n≥2, Error bars represent SD,
770 *p<0.05 (Welch's t-Test). (*I*) Pie chart depicting sources of H3K9me1 during SAM depletion. (*J*)
771 Scatter plot of 373 cytoplasmic proteins identified by LC-MS/MS with significant incorporation of
772 L-Arg $^{+0}$ that were also significantly upregulated after 24 hours of Met-restriction in 0.1% DMSO
773 treated HCT116 cells. n=4, Statistical significance of p<0.05 (Welch's t-Test). See also Table
774 S1, Table S3, and Figure S3.
775
776 Figure 4. H3K9me1 is Redistributed Over Repetitive and Transposable Elements During SAM
777 Depletion
778
779 (*A*-*B*) Bar graphs illustrating percent changes in H3K9 PTM peak number at various annotated
780 loci after 24 hours of Met-restriction in HCT116 cells. (*C*-*D*) Plots depicting changes in
781 normalized H3K9 PTM ChIP-sequencing reads to loci of lost H3K9me3 after 24 hours of Met-
782 restriction in HCT116 cells. (*E*) Bar graphs illustrating percent changes in loci annotation for
783 regions of lost H3K9me3 experiencing increased relative to decreased H3K9me1 ChIP read
784 enrichment after 24 hours of Met-restriction in HCT116 cells. (*F*) Representative ChIP-
785 sequencing track image.
786
787 Figure 5. *De novo* H3K9 Mono-methylation Preserves Heterochromatin Stability
788
789 (*A*) Bar graph illustrating the percent abundances of 5 distinct nucleosome species following
790 MNase digestion of HCT116 cells. n≥3, error bars represent SD, *p<0.05 (Welch's t-Test). (*B*)
791 Representative DNA agarose gel image of those used for the quantification presented in Figure
792 5A. (C-*E*) Bar graphs illustrating relative mRNA abundances of *LINE* 1, *HERV-K,* and *HERV-R*
793 in HCT116 cells as measured by RT-qPCR. n≥4, error bars represent SD, *p<0.05 (Welch's t-
794 Test). See also Table S2.
795
796 Figure 6. Adaptive H3K9 Mechanisms Support Epigenetic Persistence Upon Metabolic
797 Recovery
798

799 (*A*) Diagram illustrating the experimental design for replenishing Met and SAM availability after
800 24 hours of Met-restriction coupled with acute 5 μM UNC0642 or 0.1% DMSO treatment in
801 HCT116 cells. (*B*) Heatmap of $\log_2$ fold-change stoichiometric values for histone H3 and H4
802 peptides as measured by LC-MS/MS. n=4, *p<0.05, **p<0.01 (Welch's t-Test). (*C-E*) Bar graphs
803 illustrating $\log_2$ fold-changes for individual H3K9 PTMs in HCT116 cells as measured by LC-
804 MS/MS. n=4, error bars represent SD, *p<0.05 (Welch's t-Test). (*F*) PCA diagram of TPM
805 values. (*G*) EBseq multiple condition comparison diagram. (*H*) Pie chart illustrating percent
806 allocation of genes identified via RNA-sequencing to all EBseq patterns. (*I-J*) Scatter plots
807 illustrating NES and FDR q-value for GSEA identified GO terms. (*K-L*) Representative GSEA
808 running enrichment score figures. See also Table S1 and Figure S4.
809
810 Figure 7. Adaptive and Persistent Epigenetic Responses to SAM Depletion are Robust *in vivo*,
811 Independent of Age
812
813 (*A*) Diagram depicting the experimental design for *in vivo* Met-restriction of 6- and 22-month
814 C57BL/6J mice followed by dietary Met-reintroduction. (*B*) Heatmap of $\log_2$ fold-change
815 stoichiometric values for histone H3 and H4 peptides in C57BL/6J liver relative to age-matched
816 controls as measured by LC-MS/MS. n≥5, *p<0.05, **p<0.01 (Welch's t-Test). (*C*) Bar graph
817 illustrating $\log_2$ fold-changes for individual H3K9 PTMs in liver from Met-restricted C57BL/6J
818 mice relative to age-matched controls as measured by LC-MS/MS. n≥5, error bars represent
819 SD, *p<0.05 (Welch's t-Test). (*D-E*) Bar graphs illustrating relative mRNA abundances of *LINE*
820 *1*, *SINE B1*, and *SINE B2* in C57BL/6J liver as measured by RT-qPCR. n≥5, error bars
821 represent SD, *p<0.05 (Student's t-Test). (*F*) Bar graph illustrating $\log_2$ fold-changes for
822 individual H3K9 PTMs in liver from C57BL/6J relative to age-matched controls as measured by
823 LC-MS/MS. n≥5, error bars represent SD, *p<0.05, (Welch's t-Test). (*G-H*) Bar graphs
824 illustrating relative mRNA abundances of *LINE 1*, *SINE B1*, and *SINE B2* in C57BL/6J liver as
825 measured by RT-qPCR. n≥5, error bars represent SD, *p<0.05 (Student's t-Test). See also
826 Table S1, Table S2, and Figure S5.
827

828 **Supplemental Figure Titles and Legends**

829

830 Figure S1, Related to Figure 1

831

832 (*A-D*) Scatter plots of relative abundance values for key Met-cycle metabolites in HCT116 cells
833 as measured by LC-MS. n=5, error bars represent SD, *p<0.05 (Welch's t-Test). (*E-J*)
834 Correlation plots of LC-MS/MS generated $\log_2$ fold-change stoichiometric values for individual
835 histone H3 peptide proteoforms. n≥3. See also Table S1.

836

837 Figure S2, Related to Figure 2

838

839 *(*A) Diagram illustrating the experimental design for determining the conservation of H3K9
840 regulation in response to SAM depletion across various biological systems. (*B-F*) Bar graphs
841 illustrating $\log_2$ fold-changes for individual H3K9 in response to *in vitro* SAM depletion. n=3, error
842 bars represent SD, n=3, *p<0.05 (Welch's t-Test). See also Table S1.

843

844 Figure S3, Related to Figure 3

845

846 (*A-C*) Scatter plots of relative HMT mRNA abundance in HCT116 cells as measured by RT-
847 qPCR. n=4, error bars represent SD, *p<0.05 (Welch's t-Test). (*D*) Heatmap of $\log_2$ fold-change
848 stoichiometric values for unique histone H3K9 peptide proteoforms in HCT116 cells. n=4,
849 *p<0.05 (Welch's t-Test). (*E*) Scatter plot of relative cell counts for attached HCT116 cells. n=4,
850 error bars represent SD, *p<0.05 (Welch's t-Test). (F) Bar graph of relative H3K9me1
851 abundance in HCT116 cells as measured by western blot with accompanied representative blot
852 image. See Document S1 for REVERT Total Protein Stain image used for normalization. Error
853 bars represent SD, n≥3, *p<0.05 (Welch's t-Test). (*G*) Bar graphs illustrating $\log_2$ fold-changes
854 for individual H3K9 PTMs. n≥3, *p<0.05 (Welch's t-Test). (*H*) Bar graph showing average
855 incorporation of L-Arg^{+10} in H3K9 peptide proteoforms. n=4, error bars represent SD. (*I*) Density
856 plot illustrating the percentage of Met residue frequency in the primary amino acid sequence of
857 all identified cytoplasmic proteins as well as those determined to be preferentially translated.
858 See also Table S1, Table S2, and Table S3.

859

860 Figure S4, Related to Figure 6

861

862 (*A*) GSEA heatmap of relative gene expression across positive NES GO terms for Pattern 2. (B)
863 GSEA set-to-set heatmap illustrating gene enrichment overlap across positive NES GO terms
864 for Pattern 2. (*C*) GSEA heatmap of relative gene expression across negative NES GO terms
865 for Pattern 2. (D) GSEA set-to-set heatmap illustrating gene enrichment overlap across negative
866 NES GO terms for Pattern 2.
867
868 Figure S5, Related to Figure 7
869
870 (*A-E*) Bar graphs illustrating $\log_2$ fold-changes for individual H3K4, H3K18/K23, H3K27, H3K36,
871 and H4 PTMs in liver from Met-restricted C57BL/6J mice relative to age-matched controls as
872 measured by LC-MS/MS. n≥5, error bars represent SD, *p<0.05 (Welch's t-Test). (F) Bar graph
873 illustrating changes in fat, lean mass, and total body mass (BW) after 3 weeks of control or Met-
874 restricted diet feeding. n=14, error bars represent SEM, *p<0.05 (two-way ANOVA). (*G*)
875 Glucose tolerance test in 6- and 22-month C57BL/6J mice after 2 weeks of control or Met-
876 restricted diet feeding. n=14, error bars represent SEM, *p<0.05 (two-way ANOVA). (*H*) Bar
877 graph illustrating changes in fat, lean mass, and total body mass (BW) after 5 weeks of control
878 diet feeding following either 3 weeks of control or Met-restricted diet feeding. n≥6, error bars
879 represent SEM, *p<0.05 (two-way ANOVA). (*I*) Glucose tolerance test in 6- and 22-month
880 C57BL/6J mice after 4 weeks of control diet feeding following either 3 weeks of control or Met-
881 restricted diet feeding. n≥7, error bars represent SEM, *p<0.05 (two-way ANOVA). See also
882 Table S1 and Table S2.
883
884 **Star Methods Text**
885
886 Contact for Reagent and Resource Sharing:
887
888 Further information and requests for resources and reagents should be directed to and will be
889 fulfilled by the Lead Contact, John M. Denu (john.denu@wisc.edu).
890
891 Experimental Model and Subject Details
892
893 *Animals and Diets:*
894

895 All experiments involving animals were approved by the Institutional Animal Care and Use
896 Committee of the William S. Middleton Memorial Veterans Hospital, Madison WI. To test the
897 effect of Met deprivation in the context of young mice, 9-week-old male C57BL/6J mice were
898 purchased from The Jackson Laboratory (Bar Harbor, ME, USA) and placed on either an amino
899 acid defined Control diet (TD.01084, Envigo, Madison, WI, USA) or a Met-deficient diet
900 (TD.140119, Envigo, Madison, WI, USA) their respective diets at 14 weeks of age; full diet
901 compositions for these diets have been previously described (PMID: 29401631). After 5 weeks
902 on the diet, mice were sacrificed following an overnight fast and liver was flash frozen for
903 analysis as described.
904
905 To compare the effect of Met restriction on young and old mice, C57BL/6J. Nia male mice were
906 obtained from the National Institute on Aging Aged Rodent Colony, and housed in our animal
907 facility for 3-4 months until reaching 5 and 21 months of age. All animals were then placed on
908 the Control diet (TD.01084) for 4 weeks, until the mice were 6 and 22 months of age. Mice were
909 then randomized to either remain on the Control diet, or were placed on the Met-deficient diet
910 (TD.140119) for three weeks. Liver was collected and flash-frozen in liquid nitrogen harvested
911 from mice euthanized after an approximately 16-hour fast.
912
913 *Cell Lines:*
914
915 HCT116, HEK-293, HEK-293T, HMCF7, Panc1, HepG2, and HepA1 cell lines were cultured at
916 37ºC with 5.0% CO_2.
917
918 Method Details
919
920 *Metabolite Extraction:*
921
922 For HCT116 cells, ~1.5x10^6 cells were quickly rinsed 3 times with 1.5 ml ice-cold PBS pH 7.4
923 before the addition of 1.5 ml of -80ºC 80:20 MeOH:H_2O extraction solvent. Cells were incubated
924 with extraction solvent at -80ºC for 15 minutes. Next, cells were scraped off their dish and
925 transferred into a 2 ml microcentrifuge Eppendorf tube which was followed by a 5-minute,
926 maximum speed centrifugation at 4ºC. The supernatant was transferred to a new 2 ml
927 microcentrifuge Eppendorf tube. Next, 0.5 ml extraction solvent was added to the remaining
928 pellet, vortexed, and again centrifugated at maximum speed for 5 minutes at 4ºC. The 2

929 supernatants from each extraction were pooled and dried completely using a Thermo Fisher
930 Savant ISS110 SpeedVac. Dried metabolite extracts were resuspended in 80 μl of 85%
931 acetonitrile following microcentrifugation for 5 minutes at maximum speed at 4°C to pellet any
932 remaining insoluble debris. The supernatant was then transferred to a glass vial for LC-MS
933 analysis.
934
935 For *M. musculus* liver tissue, an average tissue weight of 75 mg was powdered in liquid nitrogen
936 using a mortar and pestle. Powdered tissue was transferred to an individual 1.5 ml
937 microcentrifuge Eppendorf tube and incubated with 1 ml -80°C 80:20 MeOH:H_2O extraction
938 solvent on dry ice for 5 minutes post-vortexing. Tissue homogenate was centrifugated at
939 maximum speed for 5 minutes at 4°C. Supernatant was transferred to a 15 ml tube after which
940 the remaining pellet was resuspended in 0.8 ml -20°C 40:40:20 ACN:MeOH:H_2O extraction
941 solvent and incubated on ice for 5 minutes. Tissue homogenate was again centrifugated at
942 maximum speed for 5 minutes at 4°C after which the supernatant was pooled with the
943 previously isolated metabolite fraction. The 40:40:20 ACN:MeOH:H_2O extraction was then
944 repeated as previously described. Next, 550 μl of pooled metabolite extract for each sample
945 was transferred to a 1.5 ml microcentrifuge Eppendorf tube and completely dried using a
946 Thermo Fisher Savant ISS110 SpeedVac. Dried metabolite extracts were resuspended in 450 μl
947 of 85% ACN following microcentrifugation for 5 minutes at maximum speed at 4°C to pellet any
948 remaining insoluble debris. Supernatant was then transferred to a glass vial for LC-MS analysis.
949
950 *LC-MS Metabolite Analysis:*
951
952 Each prepared metabolite sample was injected onto a Thermo Fisher Scientific Vanquish
953 UHPLC with a Waters XBridge BEH Amide column (100 m x 2.1 mm, 3.5 μm) coupled to a
954 Thermo Fisher Q-Exactive mass spectrometer. Mobile phase (A) consisted of 97% H_2O, 3%
955 ACN, 20 mM ammonium acetate, and 15 mM ammonium hydroxide pH 9.6. Organic phase (B)
956 consisted of 100% ACN. Metabolites were resolved using the following linear gradient: 0 min,
957 85% B, 0.15 ml/min; 1.5 min, 85% B, 0.15 ml/min; 5.5 min, 40% B, 0.15 ml/min; 10 min, 40% B,
958 0.15 ml/min; 10.5 min, 40% B, 0.3 ml/min; 14.5 min, 40% B, 0.3 ml/min; 15 min, 85% B, 0.15
959 ml/min; 20 min, 85% B, 0.15 ml/min. The mass spectrometer was operated in positive ionization
960 mode with a MS1 scan at resolution = 70,000, automatic gain control target = 3 x 10^6, and scan
961 range = 60-186 m/z and 187-900 m/z. This protocol was adapted from Mentch et al., 2015.
962 Individual metabolite data were called using MAVEN (Melamud et al., 2010; Clasquin et al.,

963 2012) with retention times empirically determined in-house. Peak Area Top values were
964 analyzed to determine metabolite expression.
965
966 *LC-MS DNA Methylation Assay:*
967
968 500 ng of cytosine, 5mC, and 5hmC double-stranded DNA standards from Zymo Research
969 were incubated with Zymo Research DNA Degradase Plus for 3 hours at 37°C following enzyme
970 inactivation at 70°C for 20 minutes. 75 μl of ACN was added to each standard reaction to bring
971 the final volume to 100 μl. DNA standards were centrifugated at 21,100xg for 5 minutes at 4°C
972 after which 75 μl of supernatant was transferred to a glass vial for LC-MS analysis. A range of
973 0.1 to 100 ng of digested DNA was analyzed via LC-MS to determine each nucleoside's linear
974 range of detection.
975
976 Genomic DNA extracted using a Promega Wizard Genomic DNA Purification Kit after which 1
977 μg was incubated with Zymo Research DNA Degradase Plus at 37°C following enzyme
978 inactivation at 70°C for 20 minutes. 175 μl of ACN was added to each reaction to bring the final
979 volume to 200 μl. DNA samples were centrifugated at 21,100xg for 5 minutes at 4°C after which
980 150 μl of supernatant was transferred to a glass vial for LC-MS analysis.
981
982 Each prepared nucleoside sample was injected onto a Thermo Fisher Scientific Vanquish
983 UHPLC with a Waters XBridge BEH Amide column (100 m x 2.1 mm, 3.5 μm) coupled to a
984 Thermo Fisher Q-Exactive mass spectrometer run in positive ionization mode. Mobile phase (B)
985 consisted of H_2O, 3% ACN, 20 mM ammonium acetate, and 15 mM ammonium hydroxide pH
986 9.6. Organic phase (B) consisted of 100% ACN. Nucleosides were resolved using the following
987 linear gradient: 0 min, 85% B, 0.15 ml/min; 1.5 min, 85% B, 0.15 ml/min; 5.5 min, 40% B, 0.15
988 ml/min; 10 min, 40% B, 0.15 ml/min; 10.5 min, 40% B, 0.3 ml/min; 14.5 min, 40% B, 0.3 ml/min;
989 15 min, 85% B, 0.15 ml/min; 20 min, 85% B, 0.15 ml/min. The mass spectrometer was operated
990 in positive ionization mode with a MS1 scan at resolution = 70,000, automatic gain control target
991 = 3×10^6, and scan range = 200-300 m/z, followed by a DDA scan with a loop count of 5. DDA
992 settings were as follows: window size = 2.0 m/z, resolution = 17,500, automatic gain control
993 target = 1×10^5, DDA maximum fill time = 50 ms, and normalized collision energy = 30. This
994 protocol was adapted from Mentch et al., 2015. Individual metabolite data were called using
995 MAVEN (Melamud et al., 2010; Clasquin et al., 2012) with retention times empirically

996 determined in-house. Peak Area Top values were analyzed to determine metabolite expression
997 with dAdenosine being utilized for internal normalization (m/z dCytosine: 228.0978, m/z d5mC:
998 242.1135, m/z d5hmC: 258.108, m/z dAdenosine: 252.109).
999
1000 *Histone Isolation and Chemical Derivatization:*
1001
1002 Tissue culture cell pellets were resuspended in 800 μl of ice-cold Buffer A (10 mM Tris-HCl pH
1003 7.4, 10 mM NaCl, and 3 mM $MgCl_2$) supplied with protease and histone deacetylase inhibitors
1004 (10 μg/ml leupeptin, 10 μg/ml aprotinin, 100 μM phenylmethylsulfonyl fluoride, 10 mM
1005 nicotinamide, 1 mM sodium-butyrate, and 4 μM trichostatin A) followed by 80 strokes of light
1006 pestle homogenization in a 1 ml Wheaton dounce homogenizer. Cell homogenate was then
1007 transferred to a 1.5 ml microcentrifuge Eppendorf tube and centrifugated at 800xg for 10
1008 minutes at 4°C to pellet nuclei. The supernatant was either transferred to a fresh 1.5 ml
1009 Eppendorf tube or discarded. The nuclei pellet was resuspended in 500 μl ice-cold PBS pH 7.4
1010 followed by centrifugation at 800xg for 10 minutes at 4°C. The supernatant was discarded and
1011 nuclei were again washed with 500 μl ice-cold PBS pH 7.4. Pelleted nuclei were then
1012 resuspended in 500 μl of 0.4N H_2SO_4 and rotated at 4°C for 4 hours. Samples were
1013 centrifugated at 3,400xg for 5 minutes at 4°C to pellet nuclear debris and precipitated non-
1014 histone proteins. The supernatant was transferred to a new 1.5 ml Eppendorf tube after which
1015 125 μl of 100% trichloroacetic acid was added and incubated overnight on ice at 4°C. Samples
1016 were centrifugated at 3,400xg for 5 minutes at 4°C to pellet precipitated histone proteins. The
1017 supernatant was discarded, after which the precipitant was washed with 1 ml ice-cold acetone
1018 +0.1% HCl. Samples were centrifugated at 3,400xg for 2 minutes at 4°C and the supernatant
1019 was discarded. This process was repeated except precipitant was washed with 100% ice-cold
1020 acetone. Residual acetone was allowed to evaporate at room temperature for 10 minutes after
1021 which the dried precipitant was dissolved in 125 μl H_2O. Samples were then centrifugated at
1022 21,100xg for 5 minutes at 4°C to pellet any remaining insoluble debris. Supernatant containing
1023 purified histone was then transferred to a new 1.5 ml Eppendorf tube and stored at -20°C until
1024 needed for future analyses.
1025
1026 For *M. musculus* liver tissue, an average tissue weight of 50 mg was homogenized in 800μl ice-
1027 cold Buffer supplemented with protease and HDAC inhibitors (listed above) using a 1 ml
1028 Wheaton dounce homogenizer (20 strokes of the loose pestle followed by 20 strokes of the tight

1029 pestle) and strained through a 100 μM filter before being transferred to a new 1.5 ml Eppendorf
1030 tube. All remaining steps for completing the histone isolation were performed as described
1031 previously in the tissue culture isolation protocol.
1032
1033 To prepare purified histone proteins for LC-MS/MS analysis, 5 μg of histone was diluted with
1034 H_2O to a final volume of 9 μl. 1 μl of 1 M triethylammonium bicarbonate was added to each
1035 sample to buffer the solution to a final pH of 7-9. Next, 1 μl of 1:100 propionic anhydride:H_2O
1036 was added to each sample and allowed to incubate for 2 minutes at room temperature. The
1037 propionylation reaction was then quenched via the addition of 1 μl 80 mM hydroxylamine which
1038 was allowed to incubate for 20 minutes at room temperature. Next, propionylated histones were
1039 digested with 0.1 μg trypsin for 4 hours at 37°C. Upon completion of trypsin digestion, 5 μl of .02
1040 M NaOH was added to bring the final pH between 9-10. Propionylated, trypsin digested histone
1041 peptides were then N-terminally modified with 1 μl 1:50 phenyl isocyanate:ACN for 1-hour at
1042 37°C. Modified peptides were desalted and eluted-off of Empore™C18 extraction membrane.
1043 Eluted samples were dried completely using a Thermo Fisher Scientific Savant ISS110
1044 SpeedVac, resuspended in 40 μl sample diluent (94.9% H_2O, 5% ACN, .1% TFA), and
1045 transferred into glass vials for LC-MS/MS analysis.
1046
1047 *Histone Proteomics Analysis:*
1048
1049 Derivatized histone peptides were injected onto a Dionex Ultimate3000 nanoflow HPLC with a
1050 Waters nanoEase UPLC C18 column (100 m x 150 mm, 3μm) coupled to a Thermo Fisher Q-
1051 Exactive mass spectrometer at 700 nL/ min. Aqueous phase (A) consisted of H_2O + 0.1% formic
1052 acid while the mobile phase (B) consisted of acetonitrile + 0.1% formic acid (B). Histone
1053 peptides were resolved using the following linear gradient: 0 min, 2.0% B; 5 min, 2.0% B; 65
1054 min, 35% B; 67 min, 95% B; 77 min, 95% B; 79 min, 2.0% B; 89 min, 2.0% B. Data was
1055 acquired using data-independent acquisition (DIA) mode. The mass spectrometer was operated
1056 with a MS1 scan at resolution = 35,000, automatic gain control target = 1 x 10^6, and scan range
1057 = 390-910 m/z, followed by a DIA scan with a loop count of 10. DIA settings were as follows:
1058 window size = 10 m/z, resolution = 17,500, automatic gain control target = 1 x 10^6, DIA
1059 maximum fill time = AUTO, and normalized collision energy = 30.
1060

1061 DIA Thermo .raw files were imported into Skyline open source proteomics software (MacLean et
1062 al., 2010) and matched against a pre-constructed peptide database containing unique peptide
1063 proteoforms from H3 and H4. The identity of each individually called peak was verified by hand
1064 after which total MS1 peak area values were exported for downstream analyses. To control for
1065 differences in ionization efficiencies across histone peptides, all peptides possessing an
1066 identical primary sequence were analyzed as a peptide family which enabled the calculation of
1067 stoichiometric values for each unique peptide proteoform within the family. Stoichiometric values
1068 were compared across conditions to identify altered histone peptide abundances. Furthermore,
1069 combinatorial peptide stoichiometry values were deconvoluted by totaling the stoichiometry
1070 values for all peptides possessing a given PTM independent of any other PTMs that may be
1071 present on other residues of the same primary peptide. A Welch's T-Test with a p-value cutoff of
1072 0.05 was used to determine statistical significance.
1073
1074 Hierarchical clustering was performed in MATLAB R2016a using the 'clustergram' command.
1075 Pearson's Correlation Coefficients were calculated in MATLAB R2016a using the 'corr'
1076 command.
1077
1078 *RNAi Mediated Inhibition of MAT2A and H3K9 HMT Expression:*
1079
1080 For 35 mm tissue culture dishes, $1.5x10^5$ HCT116 cells were reverse transfected with 30 pmol
1081 of targeted or control RNAi using 5 μl of Lipofectamine RNAiMAX in addition to 500 μl Opti-
1082 MEM and 2.5 ml RPMI-1640 +10% FBS. MAT2A-RNAi treated HCT116 cells used for LC-MS
1083 metabolite analysis were cultured using dialyzed FBS.
1084
1085
1086 *Methionine Restriction of Tissue Culture Cells:*
1087
1088 All tissue culture cells were initially cultured in RPMI-1640 +10% FBS at 37ºC, 5% CO_2. One
1089 day before Met-restriction, $3.5x10^6$ cells were seeded into 100 mm tissue culture dishes. One-
1090 hour before the restriction began, RPMI-1640 was replaced with fresh, Met replete media. At the
1091 time of Met-restriction, cells were rinsed 2x with 3 ml of sterile PBS pH 7.4 followed by addition
1092 of RPMI-1640 void of Met. Any small molecule inhibitors or vehicle controls would be added at
1093 this time.
1094

1095 For experiments in which Met-restriction was followed by Met repletion, HCT116 cells were
1096 washed with PBS pH 7.4 2x to maximize small molecule inhibitor and DMSO removal before
1097 reintroduction of Met replete RPMI-1640.
1098
1099 HCT116 cells cultured for LC-MS metabolite analysis were cultured in RPMI-1640 containing
1100 10% dialyzed FBS beginning 1-hour prior to beginning Met-restriction.
1101
1102 *SILAC in Tissue Culture:*
1103
1104 197 ml of SILAC RPMI-1640 +10% DFBS void of L-Arg and L-Lys was supplemented with 50mg
1105 isotopically heavy $3C_6$ $15N_4$ L-Arg HCl and 9.43mg isotopically light L-Lys to obtain final
1106 concentrations of 1.149 mM and 0.219 mM, respectively. HCT116 cells were cultured in the
1107 SILAC media for 7 days (or 9 doubling cycles at a reported doubling time of 21 hours) after
1108 which cells were washed 3x with 5 ml PBS pH 7.4 before replacing the SILAC media with
1109 isotopically light L-Arg and L-Lys RPMI-1640 +10% DFBS void of Met. Half of the cells were
1110 treated with 5 μM UNC0642 or 0.1% DMSO at this time. Furthermore, 0-hour control HCT116
1111 cells which were never exposed to isotopically light L-Arg, Met-restricted RPMI-1640 were
1112 harvested. HCT116 cells cultured in the Met-restricted media were harvested after 24 hours.
1113
1114 *SILAC Shotgun Proteomics Analysis:*
1115
1116 50 μg of cytoplasmic protein extract from the previously described SILAC Met-restriction
1117 experiment were diluted with H_2O into a final volume of 75 μl. Next, dithiothreitol was added to
1118 each sample at a final concentration of 10 mM, followed by a 15-minute incubation at 95°C. A
1119 sonication water bath was used to resolubilize precipitated proteins post-heat denaturation.
1120 Iodoacetamide was then added to a final concentration of 20 mM, followed by a 20-minute
1121 incubation at room temperature protected from light. Alkylated proteins were precipitated with
1122 337 μl ice-cold acetone for 20 minutes at -20°C. Samples were centrifugated at 21,000xg for 15
1123 minutes at 4°C, the supernatant was discarded, and precipitated protein was resuspended in
1124 400 μl of urea buffer (2 M urea and 100 mM ammonium bicarbonate pH 8). Precipitated proteins
1125 were again solubilized using a sonication water bath. Solubilized proteins were digested into
1126 peptides using 0.8 μg trypsin at 37°C overnight. Upon digest completion, samples were desalted
1127 and eluted-off Empore™C18 extraction membrane. Eluted samples were dried completely using
1128 a Thermo Fisher Scientific Savant ISS110 SpeedVac, after which being resuspended in 50 μl

1129 sample diluent (94.9% H_2O, 5% ACN, .1% TFA) and transferred to glass vials for LC-MS/MS
1130 analysis.
1131
1132 Each prepared cytoplasmic peptide sample was injected onto a Dionex Ultimate3000 nanoflow
1133 HPLC with a Waters nanoEase UPLC C18 column (100 m x 150 mm, 3μm) coupled to a
1134 Thermo Fisher Q-Exactive mass spectrometer at 800 nL/ min. Aqueous phase (A) consisted of
1135 H_2O + 0.1% formic acid while the mobile phase (B) consisted of acetonitrile + 0.1% formic acid
1136 (B). Histone peptides were resolved using the following linear gradient: 0 min, 5.0% B; 5 min,
1137 5.0% B; 120 min, 30% B; 122 min, 95% B; 127 min, 95% B; 129 min, 5.0% B; 145 min, 5.0% B.
1138 Data was acquired using data-dependent acquisition (DDA) mode. The mass spectrometer was
1139 operated with a MS1 scan at resolution = 70,000, automatic gain control target = 1 x 10^6, and
1140 scan range = 400-1000 m/z, followed by a DDA scan with a loop count of 20. DDA settings were
1141 as follows: window size = 2.0 m/z, resolution = 17,500, automatic gain control target = 2 x 10^5,
1142 DDA maximum fill time = 150 ms, and normalized collision energy = 28.
1143
1144 *MaxQuant Proteomics Analysis:*
1145
1146 Thermo .raw DDA files were analyzed using MaxQuant v1.6.2.6 (Cox et al., 2014) using the
1147 default settings with the following exceptions: Labels: 1, Arg10; Instrument: Orbitrap; LFQ: LFQ
1148 min. ratio count: 2, LFQ min. number of neighbors: 3, LFQ average number of neighbors: 6;
1149 FASTQ File: Proteome: *H. Sapiens* Proteome ID UP000005640.
1150
1151 Identified proteins with a Q-value of 0.01 or above were removed. For the remaining proteins,
1152 LFQ light (L-Arg^{+0}) and heavy (L-Arg^{+10}) values were summed to generate LFQ total protein
1153 abundance values. LFQ light values were divided by the corresponding LFQ total value to
1154 generate a percent abundance of LFQ light species for each identified protein. Welch's t-Tests
1155 with a p-value cut off of 0.05 were used to determine significant accumulation of LFQ light
1156 species in Met-restricted HCT116 samples relative to 0-hour controls. For proteins determined
1157 to have significant LFQ light species abundance after Met-restriction, LFQ total values were
1158 used to determine the corresponding change in overall protein abundance. Up to 2 null-values
1159 were removed from replicates of an experimental group to account for missed identifications. If
1160 3 of the 4 replicates for a single experimental group contained null-values, that protein was
1161 removed from all experiment groups and therefore excluded from any downstream analyses. A

1162 Welch's t-Test with a p-value cut off of 0.05 was used to determine if an identified protein was
1163 significantly more abundant after Met-restriction relative to 0-hour controls.
1164
1165 *SILAC Histone Proteomics Analysis:*
1166
1167 Histones were isolated, chemically derivatized, and analyzed by LC-MS/MS as described in
1168 "Histone Isolation and Chemical Derivatization" and "Histone Proteomics Analysis." DDA
1169 Thermo .raw files of histone proteins with incorporated isotopically heavy $3C_6$ $15N_4$ L-Arg were
1170 used to construct an H3K9/K14 peptide library using Skyline opensource proteomics software
1171 (MacLean et al., 2010). DIA files were then matched against both isotopically heavy and light L-
1172 Arg peptide libraries after which peptide identities were confirmed by hand. MS1 intensity values
1173 for both isotopically heavy and light L-Arg peptides were summed to generate total MS1 peptide
1174 proteoform intensity values which were then used to calculate the percent of total MS1 peptide
1175 proteoform signal which was contributed by isotopically heavy peptide proteoforms. Welch's T-
1176 Tests with a p-value cutoff of 0.05 were used to determine significant differences in total MS1
1177 peptide proteoform stoichiometric values as well as the percent contribution of isotopically
1178 heavy peptide proteoforms to total peptide proteoform intensity values.
1179
1180 *Chromatin Immunoprecipitation and Sequencing:*
1181
1182 $30x10^6$ HCT116 cells were resuspended in 1 ml MNase digestion buffer (50 mM Tris-HCl pH
1183 7.6, 1 mM $CaCl_2$, and 0.2% Triton X-100) after which 330 μl of the cell suspension was
1184 aliquoted into individual 1.5 ml tubes. Each tube was treated with either 45, 52.5, or 60 units of
1185 Worthington MNase for 5 minutes at 37°C shaking at 400 rpm to generate mono-nucleosomes.
1186 MNase digestions were stopped via the addition of EDTA to a final concentration of 5mM.
1187 Digested cells were then pooled and lysed at 4°C using a Covaris S220 Focused-ultrasonicator
1188 with the following settings: Peak Power = 75, Duty Factor = 5, Cycles/Burst = 100, Duration =
1189 30" on/30" off x2. Insoluble debris was centrifugated at 10,000 rpm for 10 minutes at 4°C after
1190 which the supernatant containing prepared nucleosomes was transferred to a new tube.
1191 Glycerol was added to a final concentration of 5% prior to -80°C storage. For input controls, 43
1192 μl of prepared nucleosomes were aliquoted and saved for further processing at -80°C.
1193
1194 Next, 860 μl of prepared nucleosomes was incubated with 5 μg of the desired antibody, rotating
1195 overnight at 4°C. The nucleosome/antibody solution was added to 50 μl of prepared M-280

1196 Sheep Anti-Rabbit IgG superparamagnetic Dynabeads™ and allowed to rotate at 4ºC for 4
1197 hours. Conjugated beads were then washed for 10 minutes, rotating at 4ºC under the following
1198 conditions: 3x 1 ml RIPA (10 mM Tris pH 7.6, 1 mM EDTA, 0.1% SDS, 0.1% Na-deoxycholate,
1199 1% Triton X-100) buffer, 2x 1 ml RIPA buffer +0.3 M NaCl, 2x 1 ml LiCl buffer (0.25 M LiCl,
1200 0.5% NP-40, 0.5% Na-deoxycholate), 1x with 1 ml 1xTE +50 mM NaCl. Following the final
1201 wash, beads were centrifugated at 4ºC for 3 minutes at 960xg after which the supernatant was
1202 carefully removed and discarded.
1203
1204 To elute immunoprecipitated nucleosome species, beads were resuspended in 210 μl of elution
1205 buffer (50 mM Tris-HCl pH 8.0, 10 mM EDTA, 1% SDS) and incubated at 65ºC for 30 minutes
1206 shaking at 400 rpm. Beads were resuspended every 2 minutes via brief vortexing. Next samples
1207 were centrifugated at 16,000xg for 1 minute at room temperature after which 200 μl of
1208 supernatant was transferred to a new 1.5 ml Eppendorf tube. Eluted nucleosome species were
1209 then treated with 2 μl Thermo Fisher Scientific Proteinase K for 2 hours at 55ºC. DNA was
1210 recovered from the Proteinase K digestion using the QIAquick PCR Purification Kit.
1211
1212 DNA libraries were prepared by the University of Wisconsin-Madison Biotechnology Center
1213 using the Illumina TruSeq DNA Nano kit and then sequenced across 4 lanes of an Illumina
1214 1x100 HiSeq2500 High Throughput flowcell.
1215
1216 FASTQ files were aligned unpaired using bowtie2-2.1.0 (Langmead and Salzberg, 2012)
1217 against human genome 19. Bowtie2 output SAM files were converted to BAM files, sorted and
1218 indexed using samtools 1.5 (Li et al., 2009). Broad peaks were called from sorted BAM files
1219 using MACS2-2.1.1.20160309 (Zhang et al., 2008) with a Q-value cutoff of 0.1. Input DNA was
1220 used as the control file. All identified peaks possessing a $\log_2$ fold-change below 1.75 were
1221 discarded prior to downstream analyses. Bedtools v2.25.0 (Quinlan and Hall, 2010) was used to
1222 identify unique and overlapping across samples and also used to assign raw mapped reads to
1223 pre-specified genomic loci. Genomic loci were annotated using HOMERv4.9 (Heinz et al.,
1224 2010).
1225
1226 *Quantitative PCR:*
1227

1228 RNA was extracted from HCT116 cells using Thermo Fisher Scientific TRIzol and from liver
1229 tissue using Sigma TRI Reagent, both by following the manufacturer's instructions. The
1230 concentration and purity of RNA were determined by absorbance at 260/280 nm.
1231
1232 cDNA was prepared from 1 μg of RNA using RevertAid Reverse Transcriptase for HCT116 RNA
1233 and Superscipt III for liver RNA. Oligo dT primers were used in both cDNA synthesizing
1234 reactions.
1235
1236 HCT116 cDNA was analyzed on a Roche 480 Light Cycler System with PerfeCTa SYBR Green
1237 SuperMix while cDNA generated from liver was analyzed on an Applied Biosystems StepOne
1238 Plus instrument with Sybr Green PCR Master Mix. HCT116 cDNA qPCR reactions were
1239 normalized internally using GAPDH while liver cDNA qPCR reactions were normalized internally
1240 using actin. Primer sequences are available in Table S3.
1241
1242 *RNA sequencing*
1243
1244 RNA libraries were prepared by Novogene using NEBNext adaptors followed by paired end
1245 2x150 sequencing on their Illumina Platform. FASTQ files were trimmed using Trimmomatic
1246 v0.39 (Bolger et al., 2014) and aligned using RSEM v1.2.4 (Li et al., 2011) against the human
1247 genome 18 reference transcriptome. RSEM .genes output files were used for Ebseq
1248 EBMultiTest multiple comparison analysis (Leng et al., 2013). Gene lists associated with
1249 individual EBMultiTest patterns were further analyzed with GSEA 2 (Tamayo et al., 2005;
1250 Mootha et al., 2003)
1251
1252 *MNase Accessibility Assay:*
1253
1254 $6x10^6$ HCT116 cells were resuspended in 1 ml of digestion buffer (50 mM Tris-HCl pH 7.6, 1
1255 mM $CaCl_2$, and 0.2% Triton X-100) in addition to 15 unites of Worthington MNase. MNase
1256 treated cell suspensions were incubated for 5 minutes at 37°C shaking at 400 rpm. MNase
1257 digestions were stopped via the addition of EDTA to a final concentration of 5 mM. Digested
1258 cells were then pooled and lysed at 4°C using a Covaris® S220 Focused-ultrasonicator with the
1259 following settings: Peak Power = 75, Duty Factor = 5, Cycles/Burst = 100, Duration = 30" on/30"
1260 off x2. Insoluble debris was pelleted via centrifugation at 10,000 rpm for 10 minutes at 4°C after
1261 which the supernatant was transferred to a new tube. 150 μl of digested chromatin was treated

1262 with 2 μl of Thermo Fisher Scientific Proteinase K for 90 minutes at 55°C. DNA was then
1263 purified using the QIAquick PCR Purification Kit. Next, 1 μg of purified DNA was separated on a
1264 2% agarose gel and quantified using GelAnalyzer 2010a.
1265
1266 *Western-Blotting and Image Quantification:*
1267
1268 Protein separated on SDS-PAGE gels were transferred onto 0.2 μm nitrocellulose membrane
1269 and stained with 5 ml of LI-COR REVERT Total Protein Stain for 5 minutes at room temperature
1270 before being blocked in 0.1% fat-free milk PBS pH 7.4 for 1 hour. Primary antibodies were
1271 diluted 1:1000 in 5% fat-free milk PBST pH 7.4 and incubated with the membrane overnight at
1272 4°C. LI-COR secondary antibodies were used at a 1:15,000 dilution in 5% fat-free milk PBST pH
1273 7.4 and incubated with the membrane for 1 hour at room temperature. Membranes were imaged
1274 using an Odyssey Infrared Imager (model no. 9120). Densitometry was performed using Image
1275 Studio™ Lite software. All data was normalized to REVERT™ Total Protein Stain.
1276
1277 *In vivo Tests:*
1278
1279 For glucose tolerance tests, mice were fasted overnight for 16 hours and then injected with
1280 glucose (1 g/kg) intraperitoneally as previously described (Arriola Apelo et al., 2016). Glucose
1281 measurements were taken using a Bayer Contour blood glucose meter and test strips. Mouse
1282 body composition was determined using an EchoMRI Body Composition Analyzer (EchoMRI™,
1283 Houston, TX, USA) according to the manufacturer's procedures.
1284
1285 *Quantification and Statistical Analysis*
1286
1287 Explanations of statistical analyses and parameters are present in the main and supplemental
1288 figure legends as well as in 'Method Details" where appropriate.
1289
1290 *Data and Software Availability*
1291
1292 RNA-sequencing as well as H3K9me1 and H3K9me3 ChIP-sequencing data have been
1293 uploaded to Gene Expression Omnibus (GEO) and will be made publicly available upon
1294 manuscript publication.
1295

1296 **KEY RESOURCES TABLE**

1297

REAGENT or RESOURCE	SOURCE	IDENTIFIER
Antibodies		
Rabbit polyclonal anti-H3K9me1	Abcam	Cat#ab176880; RRID#AB_2751009
Rabbit polyclonal anti-H3K9me3	Abcam	Cat#ab8898; RRID#AB_306848
Rabbit polyclonal anti-Histone H3	Abcam	Cat#ab46765; RRID#AB_880439
Rabbit monoclonal anti-alpha Tubulin	Cell Signaling Technologies	Cat#cst2125; RRID#AB_2619646
IRDye® 800CW Goat anti-Rabbit	LI-COR Biosciences	Cat#925-32211; RRID#AB_2651127
Chemicals, Peptides, and Recombinant Proteins		
UNC0642 G9a/GLP Inhibitor	R&D Systems	Cat#5132/10
DNA Degradase Plus	Zymo Research	Cat#E2020
Lipofectamine RNAiMax	Thermo Fisher	Cat#13778030
L-Lysine-2HCl	Thermo Fisher Scientific	Cat#PI89987
L-Arginine-HCl 13C6 15N4	Thermo Fisher	Cat#PI89990
Dimethyl Sulfoxide (DMSO)	Sant Cruz Biotechnology	Cat#sc-358801
Sequencing Grade Modified Trypsin	Promega	Cat#V5113
Propionic Anhydride	Sigma-Aldrich	Cat#240311
Phenyl Isocyanate	Sigma-Aldrich	Cat#78750-25ML
Leupeptin Hemisulfate	Thermo Fisher	Cat#AAJ61188MC
Aprotinin	Gold Biotechnology	Cat#A-655-100
Phenylmethylsulfonyl Fluoride (PMSF)	Gold Biotechnology	Cat#P-470-50
Trichostatin A	Thermo Fisher	Cat#501012404
Sodium Butyrate	Sigma-Aldrich	Cat#303410-100G
Nicotinamide	Sigma-Aldrich	Cat#N3376-500G
Urea	Acros Organics	Cat#197460050
Dithiothreitol (DTT)	Gold Biotechnology	Cat#DTT100
Iodoacetamide	Sigma-Aldrich	Cat#I1149-5G

Ammonium Bicarbonate	Sigma-Aldrich	Cat#09830-500G
Micrococcal Nuclease (MNase)	Worthington Biochemical	Cat#LS004798
Proteinase K	Thermo Fisher	Cat#EO0491
TRIzol™	Thermo Fisher	Cat#15596018
TRI Reagent	Sigma-Aldrich	Cat#T9424-25ML
3M Empore C18 47mm extraction disks	Empore	Cat#2215
Atlantis dC18 NanoEase Column (3 μM, 100 μM, 150 mm)	Waters	Cat#186002209
XBridge BEH Amide Column (3.5 μM, 2.1 mm, 150mm)	Waters	Cat#186004860
Superscript III Reverse Transcriptase	Thermo Fisher	Cat#18080044
RPMI-1640	Thermo Fisher	Cat#11875119
RPMI-1640 for SILAC	Thermo Fisher	Cat#88365
RPMI-1640, no methionine	Thermo Fisher	Cat#A1451701
Fetal Bovine Serum (FBS)	Thermo Fisher	Cat#16000044
Dialyzed Fetal Bovine Serum (DFBS)	Thermo Fisher	Cat#88212
Critical Commercial Assays		
PerfeCTa SYBR® Green SuperMix	Quanta Bio	Cat#95054-02K
SYBR Green PCR Master Mix	Thermo Fisher	Cat#4309155
REVERT Total Protein Stain	LI-COR Biosciences	Cat#926-11011
RevertAid First Strand cDNA Synthesis Kit	Thermo Fisher	Cat#K1621
Wizard® Genomic DNA Purification Kit	Promega	Cat#A1120
Dynabeads™ M-280 Sheep Anti Rabbit IgG	Thermo Fisher	Cat#11203D
QIAquick PCR Purification Kit	QIAGEN	Cat#28104
TruSeq DNA Nano	Illumina	Cat#20015964
Axygen™ Light Cycler 480 Compatible PCR Plates	Thermo Fisher	Cat#14-223-212
Deposited Data		
H3K9me1 and H3K9me3 ChIP-sequencing Data	This paper	GEO Accession Number: Available upon manuscript publication
RNA-sequencing Data	This paper	GEO Accession Number: Available upon manuscript publication

Experimental Models: Cell Lines		
H. sapiens: HCT116	ATCC	CCL-247
H. sapiens: HEK-293T	ATCC	CRL-3216
H. sapiens: HEK-293	ATCC	CRL-1573
H. sapiens: HepG2	ATCC	HB-8065
H. sapiens: MCF7	ATCC	HTB-22
H. sapiens: Panc1	ATCC	CRL-1469
M. musculus: Hepa-1c1c7	ATCC	CRL-2026
Experimental Models: Organisms/Strains		
M. musculus: C57BL/6J (9-weeks of age)	The Jackson Laboratory	JAX: 000664
M. musculus: C57BL/6J (2- and 18-months of age)	The National Institute on Aging Rodent Colony	N/A
Oligonucleotides		
5-Methylcytosine and 5-Hydroxymethylcytosine DNA	Zymo Research	Cat#D505
Stealth RNAi Sense Sequence: *H. sapiens* MAT2A: 5′AUCAAGGACAGCAUCACUGAUUUGG-3′	Thermo Fisher	Kera et al., 2013
Stealth RNAi Sense Sequence: Control: 5′-AGGAGGAUAUUACCAUGGACAAGAC-3′	Thermo Fisher	Kera et al., 2013
SUV39H1 RNAi: *H. sapiens*	Novus Biologicals	H00006839-R01-20nmol
SUV39H2 RNAi: *H. sapiens*	Novus Biologicals	H00079723-R01-20nmol
SETDB1 RNAi: *H. sapiens*	Novus Biologicals	H00009869-R01-20nmol
G9a/EHMT2 RNAi: *H. sapiens*	Novus Biologicals	H00010919-R02-20nmol
GLP/EHMT1 RNAi: *H sapiens*	Novus Biologicals	H00079813-R01-20nmol
RT-qPCR Primers	See Table S2	See Table S2
Software and Algorithms		
Bowtie2-2.1.0	Langmead and Salzberg, 2012	http://bowtie-bio.sourceforge.net/bowtie2/index.shtml

Samtools 1.5	Li et al., 2009	http://samtools.sourceforge.net/
MACS2-2.1.1.20160309	Zhang et al., 2008	http://liulab.dfci.harvard.edu/MACS/
Bedtools v2.25.0	Quinlan and Hall, 2010	https://bedtools.readthedocs.io/en/latest/
HOMER v4.9	Heinz et al., 2010	http://homer.ucsd.edu/homer/
GelAnalyzer 2010a	Lazar Software	http://gelanalyzer.com/index.html
MAVEN	Melamud et al., 2010; Clasquin et al., 2012	http://genomics-pubs.princeton.edu/mzroll/index.php
MAXQUANT	Cox et al., 2014	http://www.biochem.mpg.de/5111795/maxquant
Trimmomatic v0.39	Bolger et al., 2014	http://www.usadellab.org/cms/?page=trimmomatic
RSEM v1.2.4	Li et al., 2011	https://deweylab.github.io/RSEM/
GSEA 2	Tamayo et al., 2005 Mootha et al., 2003	http://software.broadinstitute.org/gsea/index.jsp
Skyline	MacLean et al., 2010	https://skyline.ms/project/home/software/Skyline/begin.view
Other		
Control *M. musculus* Diet	Envigo	TD.01084
Methionine Deficient *M. musculus* Diet	Envigo	TD.140119

1298

1299

1300 **Supplemental File Titles and Legends**

1301

1302 Document S1, Related to Figures 3 and S3. Primary Antibody and REVERT Total Protein Stain
1303 Western Blot Membranes.

1304

1305 (*A*) Cytoplasm anti-H3K9me1 (Figure 3E). (*B*) REVERT Total Protein Stain for cytoplasm anti-
1306 H3K9me1 (Figure 3E). (*C*) Cytoplasm anti-H3 (Figure 3E). (*D*) REVERT Total Protein Stain for
1307 cytoplasm anti-H3 (Figure 3E). (*E*) Cytoplasm anti-αTubulin (Figure 3E). (*F*) REVERT Total
1308 Protein Stain for cytoplasm anti-αTubulin (Figure 3E). (*G*) Nucleoplasm anti-αTubulin (Figure
1309 3E). (*H*) REVERT Total Protein Stain for nucleoplasm anti-αTubulin (Figure 3E). (*I*) Purified
1310 histone anti-H3K9me1 (Figure S3F). (*J*) REVERT Total Protein Stain for purified histone anti-
1311 H3K9me1 (Figure S3F).

1312

1313 Table S1, Related to Figures 1-3, 6-7, S1-S3, and S5. LC-MS/MS % Abundance Histone PTM
1314 Data.

1315

1316 Table S2, Related to Figures 2, 5, 7, S3, and S5. RT-qPCR Primers.

1317

1318 Table S3, Related to Figure 3. SILAC Cytoplasmic Proteins.

1319

1320

1321

Figure 1. Methionine Restriction Stimulates Dynamic Histone PTM Response

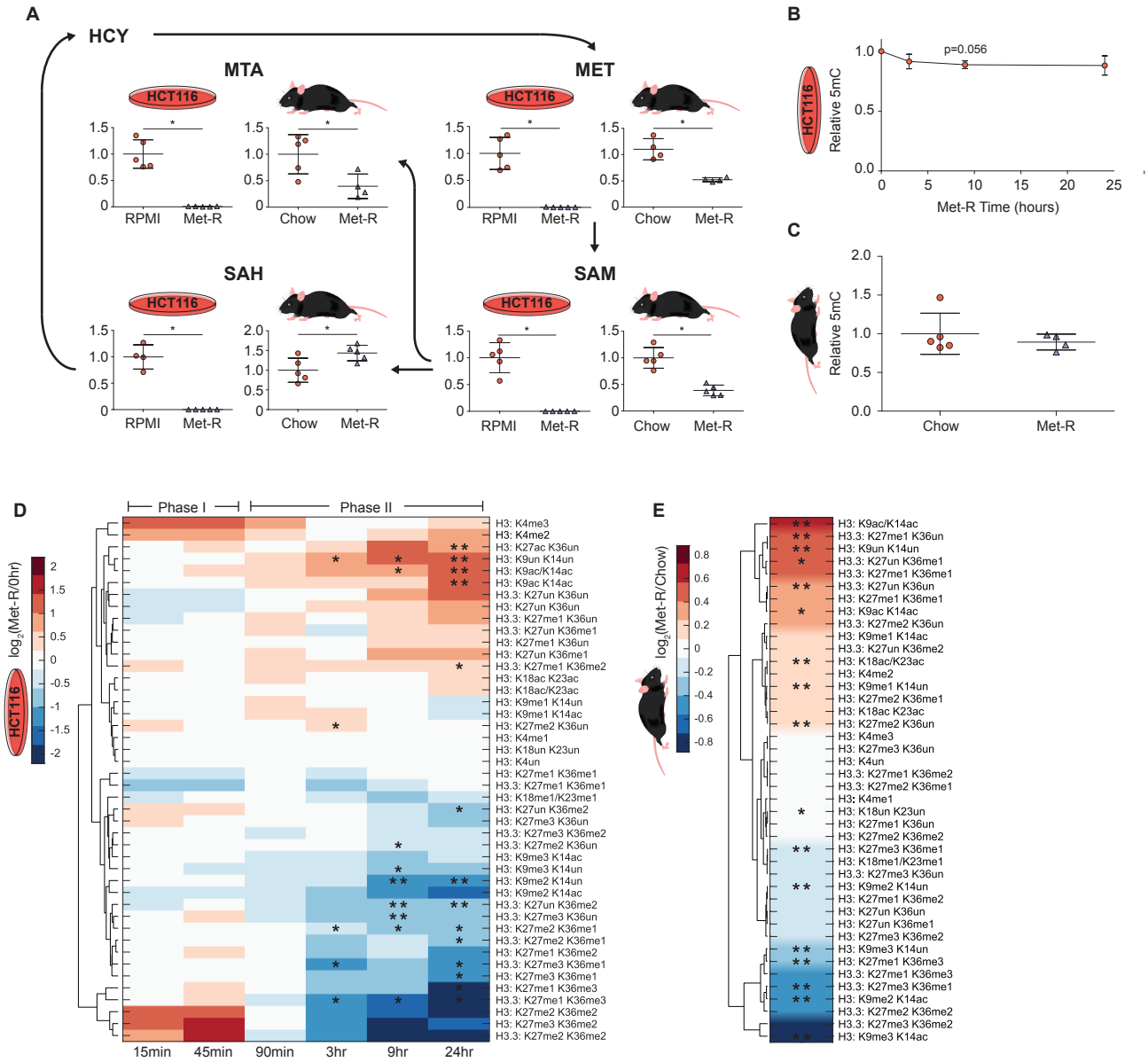

Figure 2. Decreased SAM Availability Drives Robust Histone Methylation Response

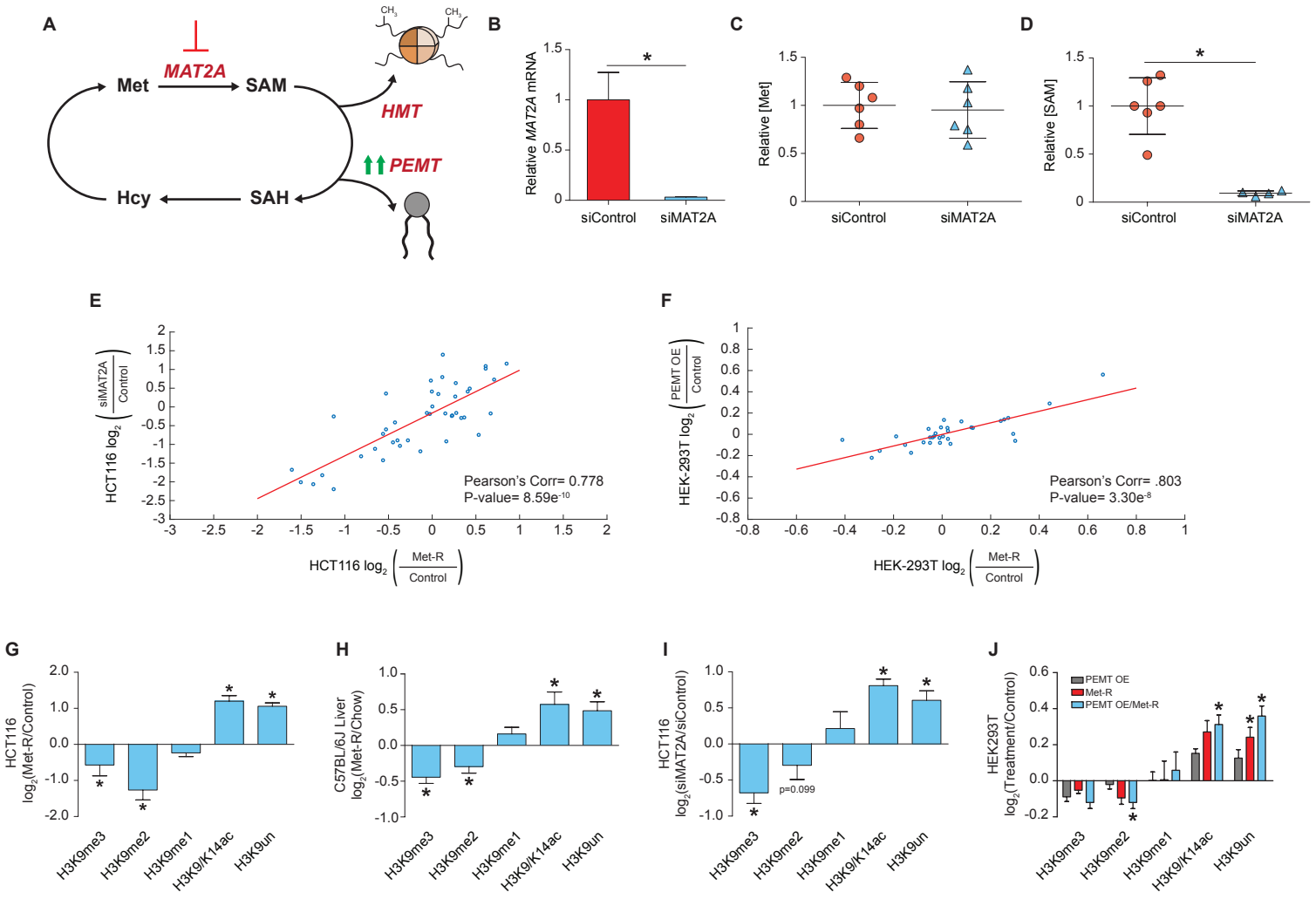

Figure 3. H3K9me1 Abundance under SAM Depletion is Driven by *de novo* Methylation

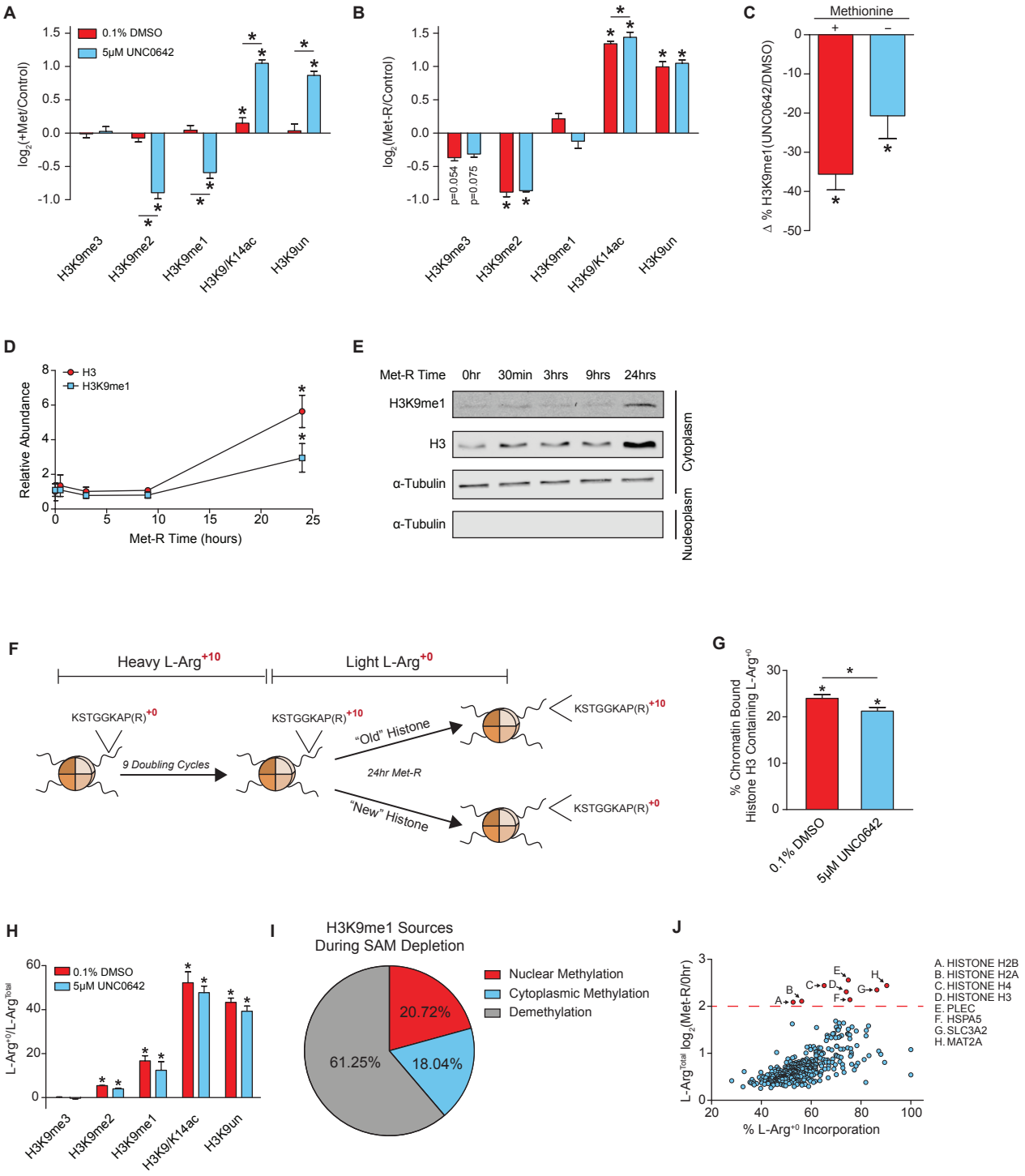

Figure 4. H3K9me1 is Redistributed Over Repetitive and Transposable Elements During SAM Depletion

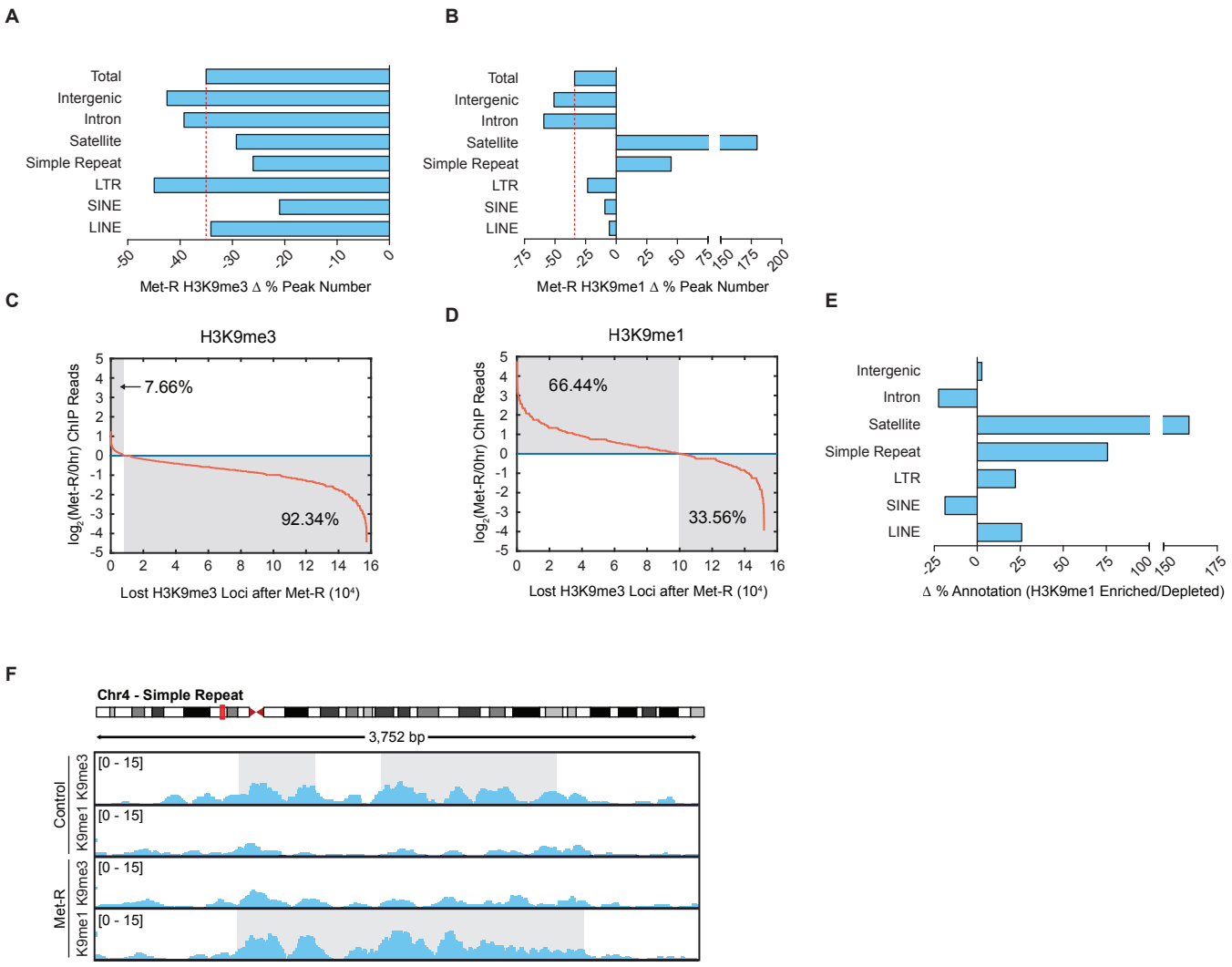

Figure 5. *De novo* H3K9 Mono-methylation Preserves Heterochromatin Stability

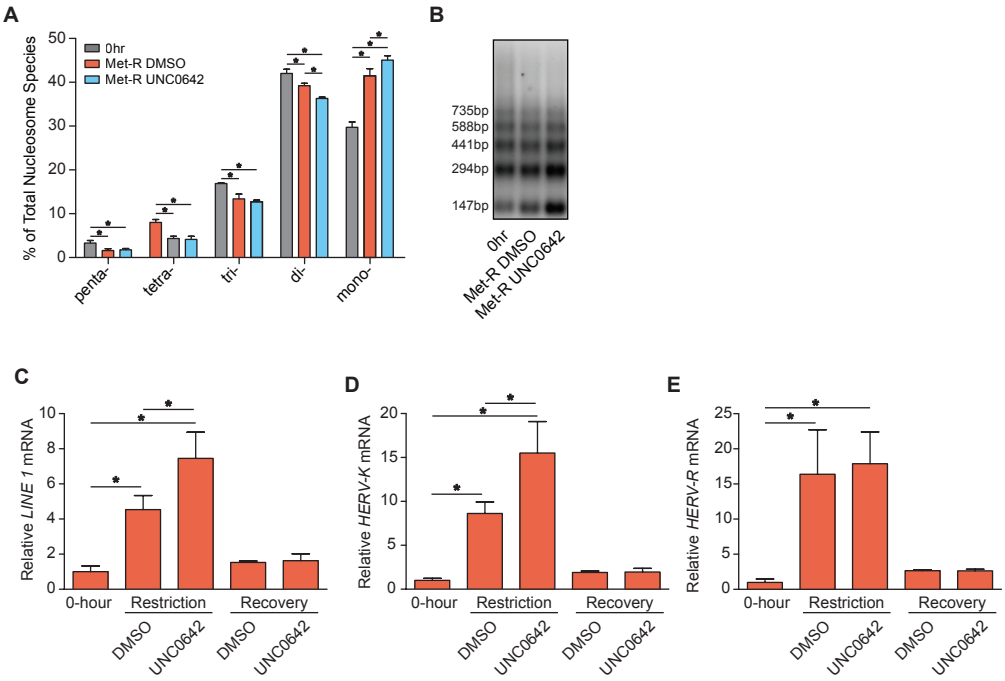

Figure 6. Adaptive H3K9 Mechanisms Support Epigenetic Persistence Upon Metabolic Recovery

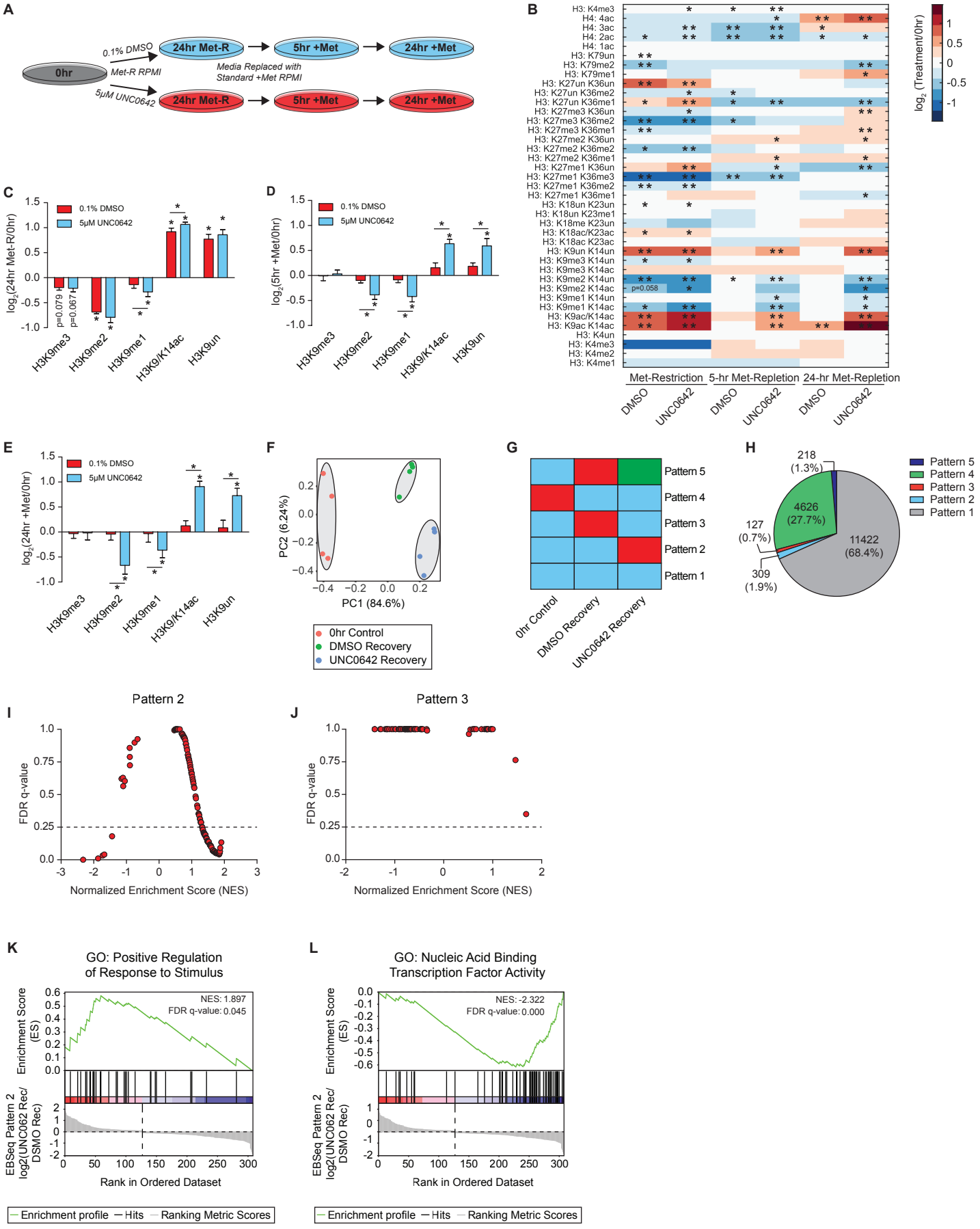

Figure 7. Adaptive and Persistent Epigenetic Responses to SAM Depletion are Robust *in vivo*, Independent of Age

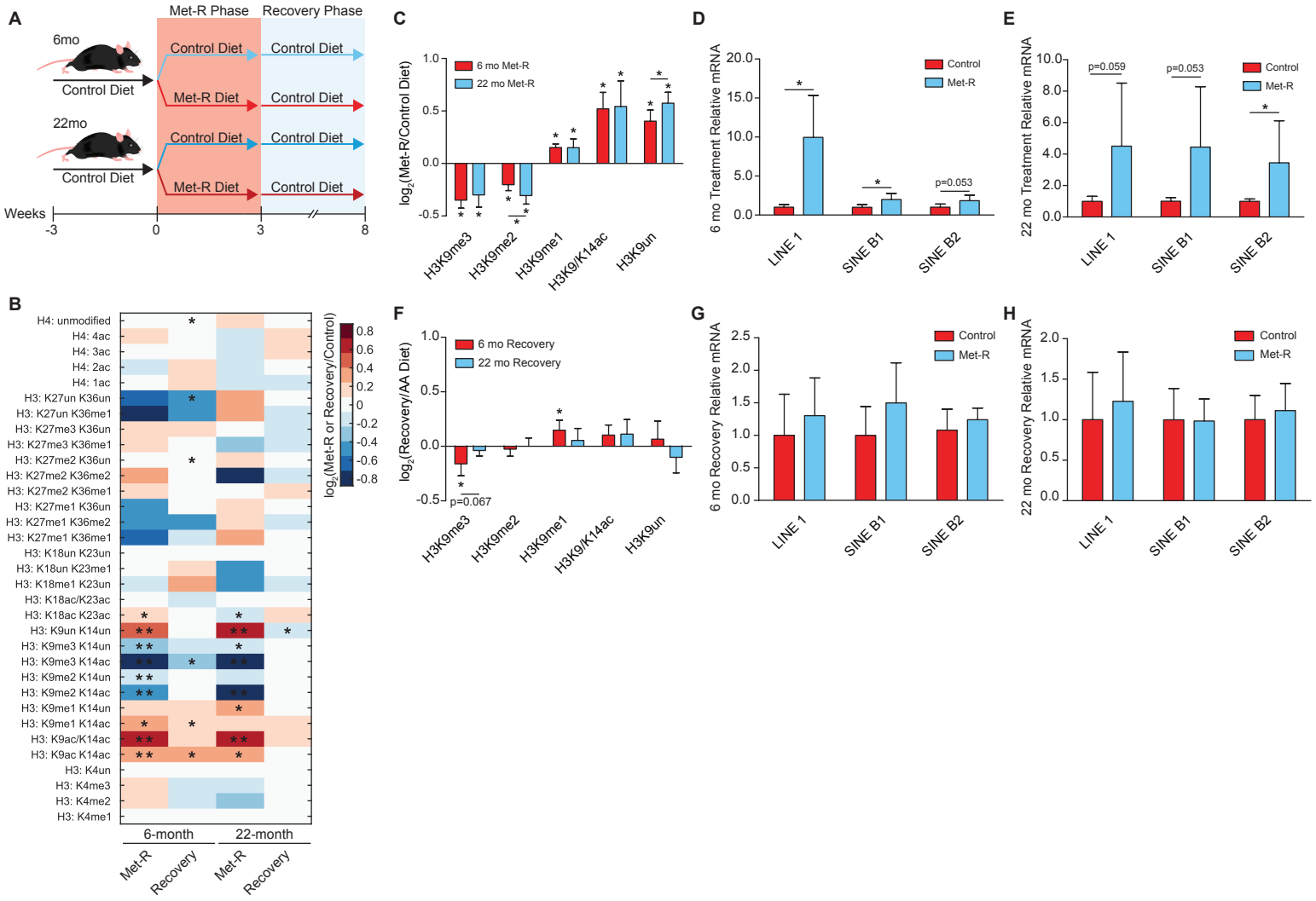

Figure S1. Related to Figure 1.

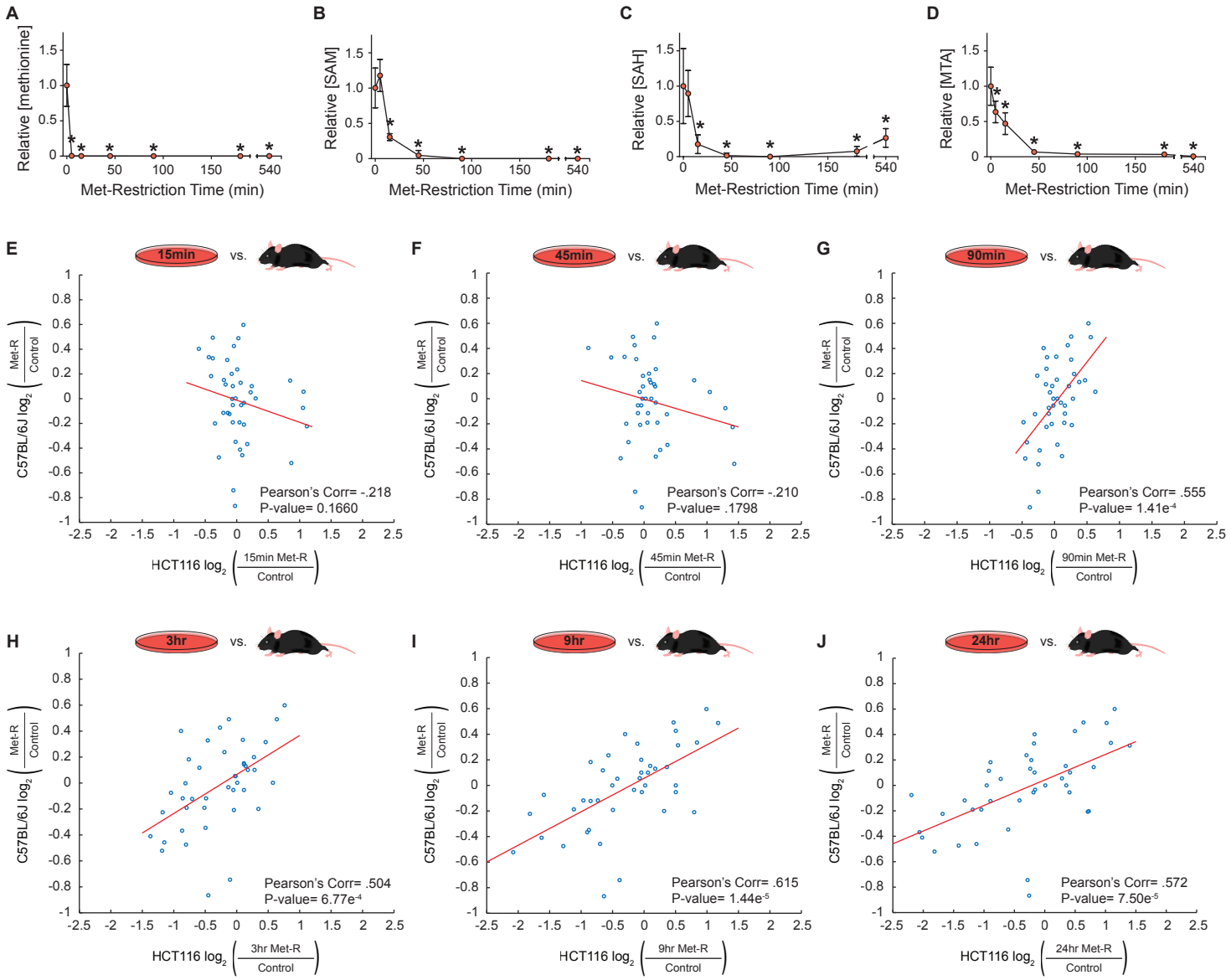

Figure S2. Related to Figure 2

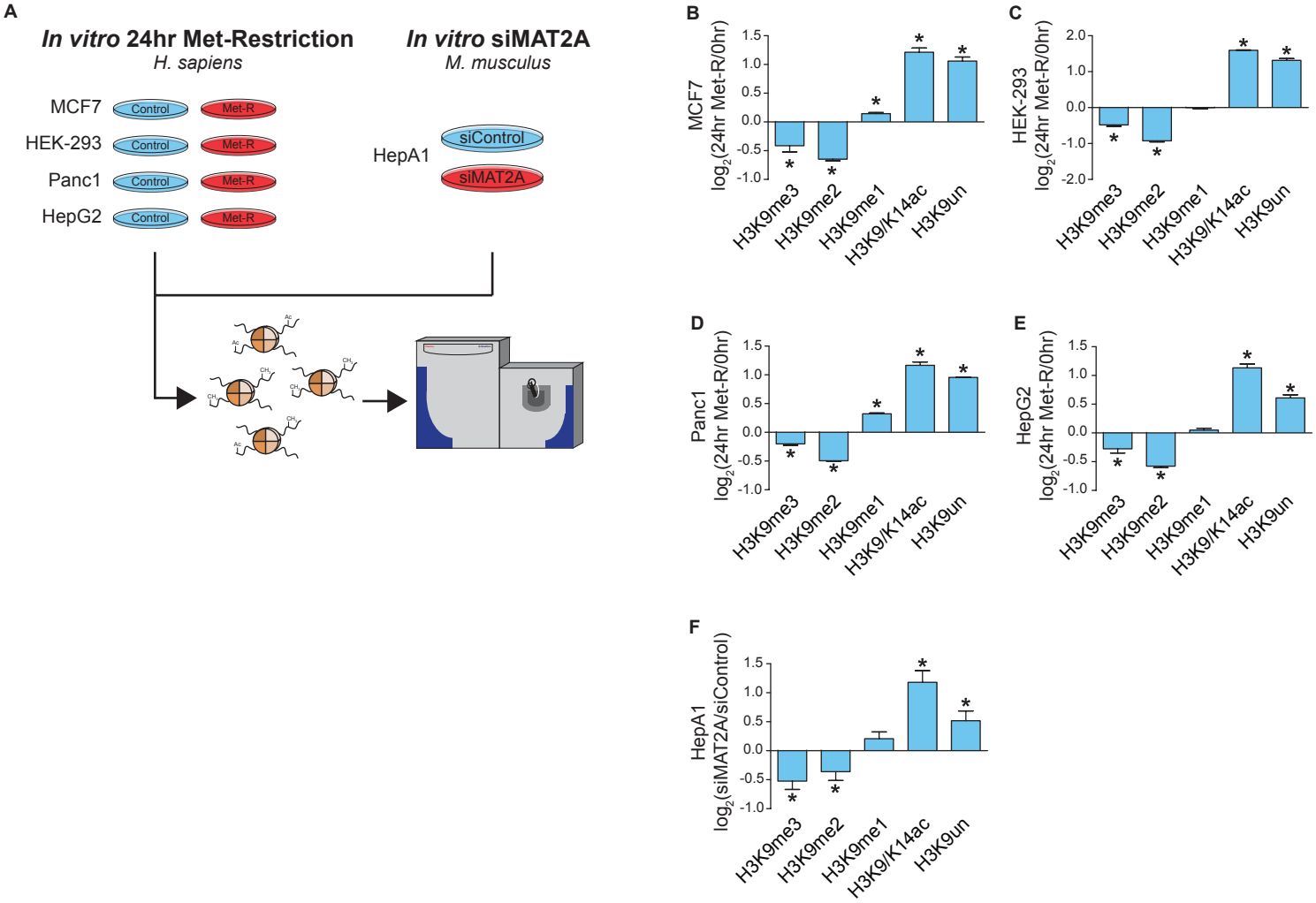

Figure S3. Related to Figure 3

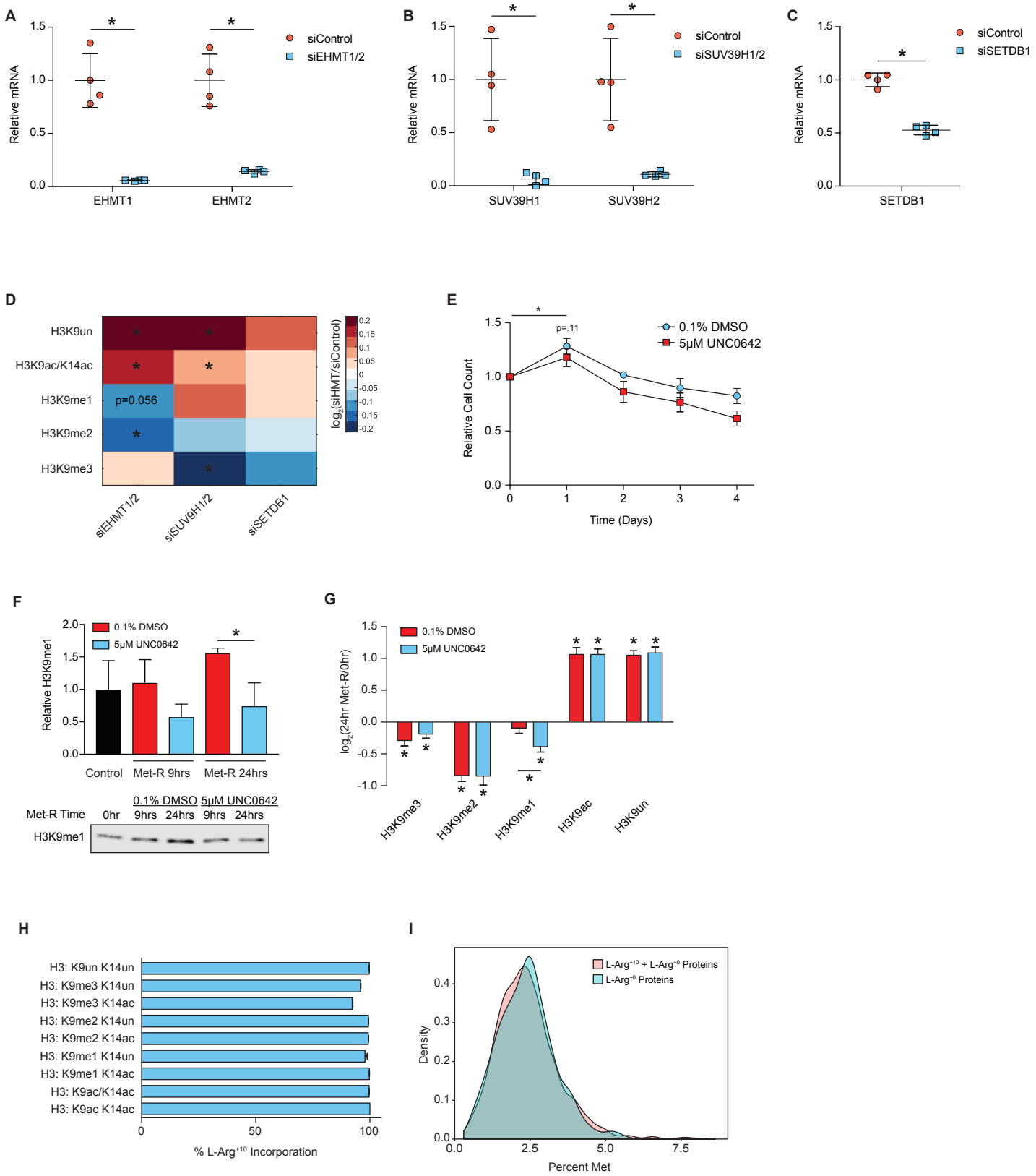

Figure S4. Related to Figure 6

A

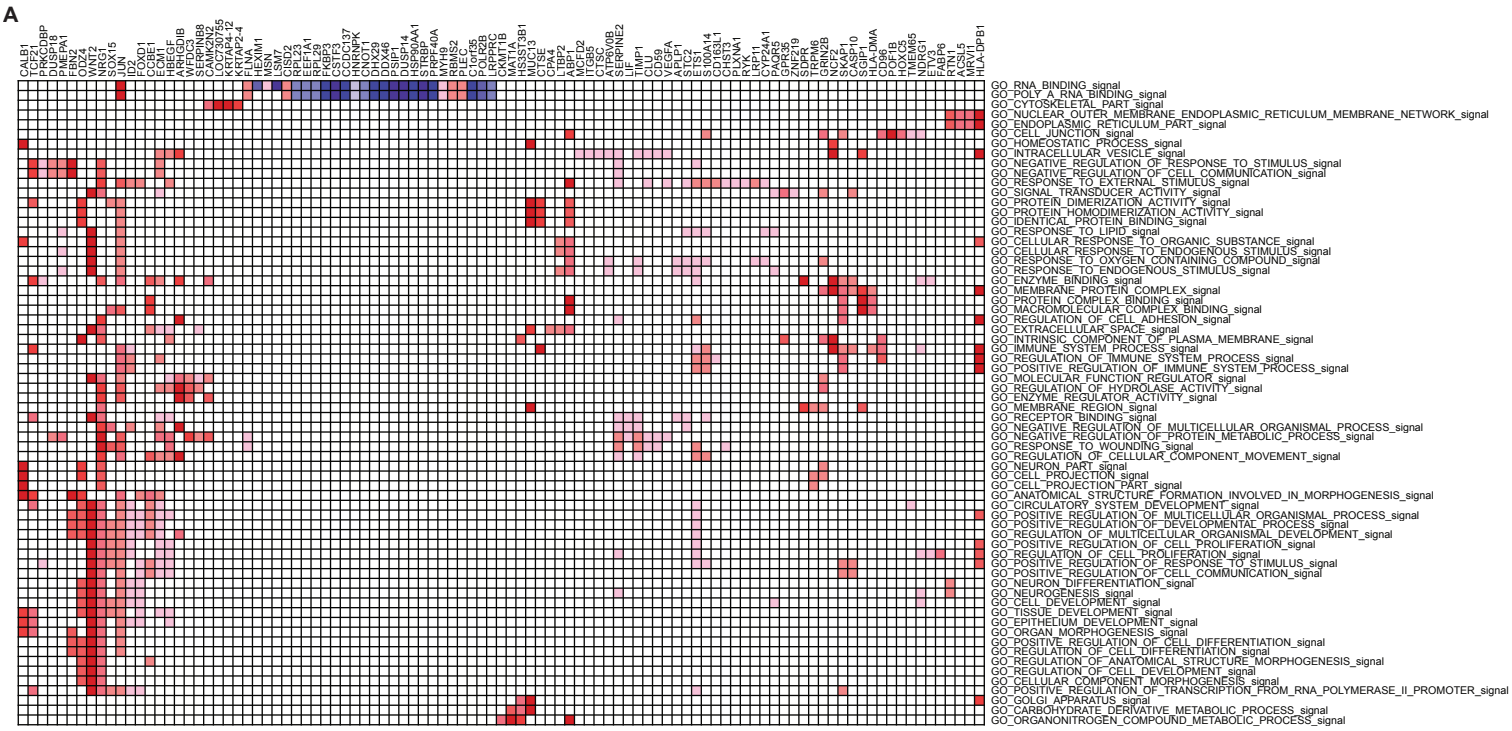

B

C

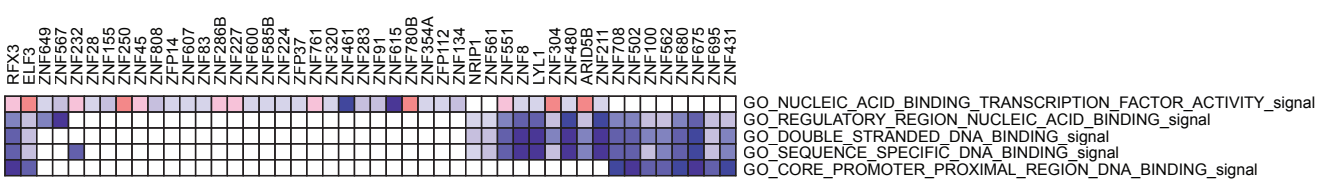
RFX3
ELF3
ZNF649
ZNF567
ZNF232
ZNF28
ZNF155
ZNF250
ZNF45
ZNF808
ZFP14
ZNF607
ZNF83
ZNF286B
ZNF227
ZNF600
ZNF585B
ZNF224
ZFP37
ZNF761
ZNF320
ZNF461
ZNF283
ZNF91
ZNF615
ZNF780B
ZNF354A
ZFP112
ZNF134
NRIP1
ZNF561
ZNF551
ZNF8
LYL1
ZNF304
ZNF480
ARID5B
ZNF211
ZNF708
ZNF502
ZNF100
ZNF562
ZNF680
ZNF675
ZNF695
ZNF431
GO_NUCLEIC_ACID_BINDING_TRANSCRIPTION_FACTOR_ACTIVITY_signal
GO_REGULATORY_REGION_NUCLEIC_ACID_BINDING_signal
GO_DOUBLE_STRANDED_DNA_BINDING_signal
GO_SEQUENCE_SPECIFIC_DNA_BINDING_signal
GO_CORE_PROMOTER_PROXIMAL_REGION_DNA_BINDING_signal

D

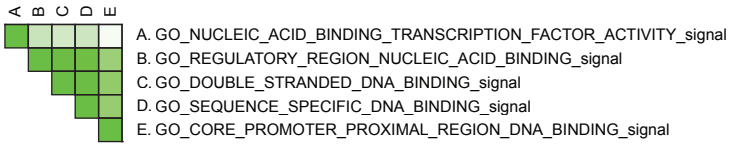
A
B
C
D
E
A. GO_NUCLEIC_ACID_BINDING_TRANSCRIPTION_FACTOR_ACTIVITY_signal
B. GO_REGULATORY_REGION_NUCLEIC_ACID_BINDING_signal
C. GO_DOUBLE_STRANDED_DNA_BINDING_signal
D. GO_SEQUENCE_SPECIFIC_DNA_BINDING_signal
E. GO_CORE_PROMOTER_PROXIMAL_REGION_DNA_BINDING_signal
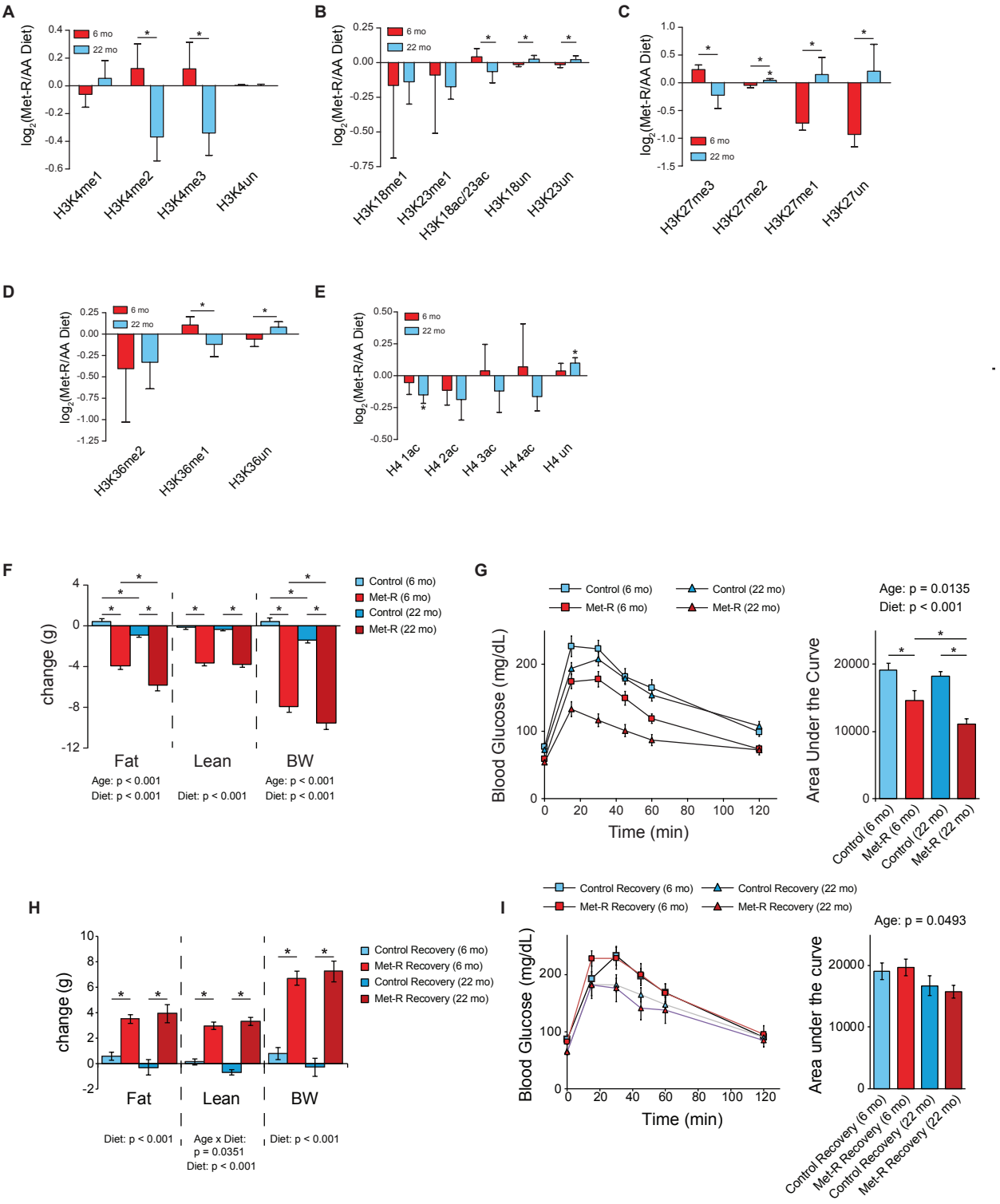
Figure S5. Related to Figure 7